Structural inheritance and hydrothermal alteration impact on fluid circulation in a clay-rich shear zone

Benjamin Avakian, Béatrice A Ledésert, Ghislain Trullenque, Ronan L Hébert, Johanne Klee, Sébastien Potel, Titouan Miloikovitch, Steven Goderis, Philippe Claeys

Journal of Structural Geology 190 (2025) 105296

Contents lists available at ScienceDirect

Journal of Structural Geology

journal homepage: www.elsevier.com/locate/jsg

Structural inheritance and hydrothermal alteration impact on fluid circulation in a clay-rich shear zone

Benjamin Avakian [a,b,c,*], Béatrice A. Ledésert [a], Ghislain Trullenque [c], Ronan L. Hébert [a], Johanne Klee [d], Sébastien Potel [c], Titouan Miloikovitch [a], Steven Goderis [b], Philippe Claeys [b]

[a] CY Cergy Paris Université, Géosciences et Environnement Cergy, 1 Rue Descartes, Neuville-sur-Oise, 95000, France
[b] Vrije Universiteit Brussel, Archaeology, Environmental Changes & Geo-Chemistry, Pleinlaan 2, Brussels, 1050, Belgium
[c] UniLaSalle, B2R (U2R 7511) UPJV-UNIL, 19 rue Pierre Waguet, 60000, Beauvais, France
[d] Lithium de France, 16 Rue des Couturières, Bischwiller, 67240, France

ARTICLE INFO

Keywords:
Fault zone
Geothermal reservoir
Black Forest
Analogue
Fluid/rock interactions
Permeability

ABSTRACT

Deep geothermal power plants in the Upper Rhine Graben (URG) harness natural hot brines circulating within the fracture network of basement rocks. The nature and geometry of the fault network must be documented in detail to reduce the risk of targeting low-permeability structures during drilling. Fault zones and associated fracture networks exhibit variable hydraulic properties depending on the nature of their deformation, hydrothermal alteration, and mineral infills. The Schauinsland mine, located on the eastern shoulder of the URG, is considered an analogue for exploited geothermal basement reservoirs. It provides a 3D exposure of a clay-rich shear zone and a perpendicular ore vein, analogous to present-day brine circulation pathway encountering a heterogeneously permeable structure. Petrophysical, petrographical, mineralogical and geochemical investigations of this shear zone offer the opportunity to reconstruct its formation and the associated fluid pathways. A statistical analysis of the dataset was carried out to highlight correlations between deformation and hydrothermal alteration processes. Through repeated seismic cycles, the core zone shifted from a conduit to a barrier for fluid circulation, due to the precipitation of secondary minerals within the remaining open spaces, resulting in a multi-core structure. Observations show that the damage zones within the transition zone of the shear zone likely constitute the optimal zone for present-day fluid circulation.

1. Introduction

The Upper Rhine Graben (URG) is renowned worldwide for its deep geothermal energy production in both France and Germany (Genter et al., 1996; Baujard et al., 2017; Vidal and Genter, 2018; Bertrand et al., 2021; Glaas et al., 2021; Frey et al., 2022). The basement and basement/sediment interface have been the main targets of geothermal plants for electricity and heat production for over 15 years. Fault zones with associated damage zones (DZ) and open fractures are of critical importance as they provide fluid flow pathways which permeability exceeds that of the matrix (Caine et al., 1996; Bense et al., 2013; Callahan et al., 2019). Therefore, after geophysical explorations, drilling operations target fault zones, whose locations are evidenced by hydrothermal alteration observed in drill cuttings and reservoir properties revealed by well log data (Genter et al., 2010; Ledésert et al., 2010; Meller and Ledésert, 2017).

Throughout the reservoir's lifetime, fluid/rock interactions and deformation processes may impact fault zones (Caine et al., 1996; Bense et al., 2013) by altering their hydraulic properties from a conduit to a barrier (Faulkner et al., 2010; Callahan et al., 2020; Klee et al., 2021b) and can either lead to a fault-valve behaviour through their seismic cycle (Sibson, 1992, 2007). Following the rupture of a fault zone after the loading of shear stress, fracturing and primary mineral dissolution result in an increase in permeability of the fault zone (Caine et al., 1996; Caine and Tomusiak, 2003) while the precipitation of secondary minerals such as clays or quartz can clog the associated fractures (Caine et al., 1996; Ledésert et al., 1999; Callahan et al., 2020). In addition, hydrothermal alteration modifies the fault zone's mechanical properties through the precipitation of secondary phases that affect the strength of the

* Corresponding author. Laboratoire Géosciences et Environement Cergy, CY Cergy Paris Université, 1 Rue Descartes, Neuville-sur-Oise, 95000, France.
E-mail addresses: benjamin.avakian@cyu.fr (B. Avakian), beatrice.ledesert@cyu.fr (B.A. Ledésert), ghislain.trullenque@unilasalle.fr (G. Trullenque), ronan.hebert@cyu.fr (R.L. Hébert), johanne.klee@lithiumdefrance.com (J. Klee), sebastien.potel@unilasalle.fr (S. Potel), titouan.miloikovitch@cyu.fr (T. Miloikovitch), steven.goderis@vub.be (S. Goderis), phclaeys@vub.be (P. Claeys).

https://doi.org/10.1016/j.jsg.2024.105296
Received 15 April 2024; Received in revised form 15 November 2024; Accepted 18 November 2024
Available online 21 November 2024

Abbreviations

URG	Upper Rhine Graben
ECRIS	European Cenozoic Rift System
BF	Black Forest
RFZ	Ruschel Fault Zone
DZ	Damage Zone
CZ	Core zone
MCZ	Main core zone
TZ	Transition zone
DRIFTS	Diffuse Reflectance Infrared Fourier Transform Spectroscopy
μXRF	Micro X-Ray Fluorescence
PCA	Principal component analysis

structure: e.g, weakening it in the case of clay crystallization (Meller and Kohl, 2014; Schuck et al., 2020) or strengthening it for quartz (Callahan et al., 2020). Repeated cycles of deformation can occur as the fault zone strengthens during the interseismic phase, leading to multiple switches from conduit to barrier behaviour (Sibson, 1992; Callahan et al., 2020). However, the precipitation of secondary phases with low friction properties such as clays might reduce the fault zone's mechanical strength, clog the porosity and localise the deformation. To maintain the highest profitability of the reservoir throughout its exploitation, clear documentation of the fault zone architecture and its internal properties is necessary to foresee the reservoir's evolution as permeability distribution may differ between single-core and multi-core fault structures (Faulkner et al., 2010; Choi et al., 2016; Torabi et al., 2020; de Joussineau, 2023; Bischoff et al., 2024).

Reservoir permeability also relies on the orientation of the fractures and other planar structures within associated fault zones. The permeability distribution within fractured rocks exhibits anisotropy associated with the component orientations in the fault zone (Caine et al., 1996). Within a DZ, high permeability is expected parallel to the core zone while the core zone presents low permeability both parallel and perpendicular to its orientation (Bense et al., 2013; Torabi et al., 2020). Moreover, in the case of foliated crystalline rocks, the mineral fabric also influences the permeability distribution in the rock. The foliation can either act as a barrier or a preferential pathway for fluid circulation if the flow is normal or perpendicular to the foliation (Acosta and Violay, 2020). Fractures need to be connected to ensure fluid flow through the reservoir and are dependent on fracture branch lengths which are associated with the effective permeability (Lahiri, 2021). The orientation of the stress field influences the behaviour of fractures, enabling them to act as preferential fluid pathways. If fractures are preferentially aligned to the maximum horizontal stress, they can dilate and control the reservoir fluid flow (Meixner et al., 2016; Acosta and Violay, 2020). Understanding the geological history of the reservoir is essential to account for these parameters.

In the URG, with the deep basement only being reached by drilling mainly performed in destructive conditions, it may be relevant to work on analogues in order to study 3D the structures responsible for fluid flow. Well log data are generally limited for the characterization of fault zone structures and samples cannot be collected easily in the reservoir apart from drilling. To better understand the behaviour of fault zones in the URG basement geothermal reservoirs regarding fluid/rock interaction, a vertical shear zone in the Black Forest (BF; Germany) exposed in a mine is studied. In this study, an analogue is defined as a geological exposure that underwent a similar geological history as an in-depth structure and that may provide clues about formation processes (Dezayes et al., 2021). Analogues are widely used to better understand underground structures for geothermal purposes (Bertrand et al., 2021; Chabani et al., 2021; Dezayes et al., 2021; Klee et al., 2021a, 2021b; Bossennec et al., 2022; Peacock et al., 2022; Schulz et al., 2022). In the case of the URG, Klee et al. (2021a,b) and Chabani et al. (2021) worked on the Noble Hills' granite analogue located in the Death Valley (California, USA). Bertrand et al. (2021); Dezayes et al. (2021) studied the Vosges massif on the western shoulder of the URG. Bossennec et al. (2022) chose the Odenwald (Germany) and characterised surface fractures as analogues of the northern URG. In the present study, the analogue is located on the eastern shoulder of the URG, was chosen to remain in the same geological context as the regional geothermal reservoirs exploited at Soultz-sous-Forêts, Rittershoffen and Illkirch in France.

This study focuses on a fossilised fault zone in a mine gallery of the Schauinsland massif in the BF. The analogue provides a 3D view of a clay-rich shear zone with a multi-core architecture, perpendicularly cut by another shear zone. Samples were collected throughout the shear zone and characterized using a multidisciplinary approach with petrophysical, petrographical, mineralogical and geochemical analyses. The terminology of the fault rock samples is defined according to Sibson (1977). Documenting the interaction between the ore vein and a multi-core shear zone contributes to understand how the permeability is distributed within the alternation of damage zones and core zones enriched in clay minerals. This analogue will provide information on the degree of deformation and hydrothermal alteration that should not be exceeded to ensure subsequent fluid flow, represented here by the ore vein, throughout the shear zone. The analogue will also help in identifying what should be the main structural features indicating potential permeability throughout the whole shear zone. On a larger scale, this information can be used in defining a target for geothermal drilling within a potential reservoir in the URG. Identifying whether or not the fault core or the damage zone should be targeted is cost-effective. This is why the damage zone of the Rittershoffen fault was specifically targeted for the ECOGI geothermal heat production purpose (Vidal et al., 2017). Moreover, ensuring a high reservoir permeability will reduce the risks of induced seismicity related to permeability enhancement during geothermal well stimulations.

2. Geological setting

The URG (Fig. 1) is part of the European Cenozoic Rift System (ECRIS) that extends from the North Sea to the Mediterranean Sea (Illies, 1967; Schumacher, 2002; Ziegler and Dèzes, 2005). It is NNE oriented, about 300 km long and 30–40 km wide and is bordered by NNE normal faults (Ziegler, 1992). Mesozoic and Cenozoic sediments that lay on top of a Variscan basement can reach up to 3.5 km thickness in the deepest part (Ziegler, 1992). The Vosges massif to the west and the BF massif to the East correspond to the shoulders of the URG and delimit the structure.

The structures inherited from the Variscan orogeny influenced the polyphasic formation of the URG (Ziegler, 1992; Schumacher, 2002). Carboniferous and Permian terranes accreted along NE to ENE Variscan dislocation zones (Schumacher, 2002). An example is given by the southeast vergent and dextrally sheared Badenweiler-Lenzkirch zone in the Black Forest (Krohe and Eisbacher, 1988). At the beginning of the Variscan orogenesis, north-oriented compression resulted in sinistral NE and dextral NW shear faults followed by an NNE extension event reactivating NW to WNW faults until the Permian. Subsequently, a Permian compression and thrust event with an NE direction is highlighted by NW dextral and East sinistral shear faults (Burg et al., 1984). Late Permian extension formed basins along NE to ENE-oriented structures (Villemin and Bergerat, 1987; Schumacher, 2002; Ziegler et al., 2006). Variscan terranes were intruded by granitoids with a NE to NNE orientation along collisional or shear zones during the Visean and Permian (Lagarde et al., 1992; Altherr et al., 1999, 2000; Edel and Schulmann, 2009).

The late-Permian extension lasted until the Jurassic. Through the Triassic, the Buntstandstein sandstones, Muschelkalk limestones and Keuper evaporites were deposited on the site of the future URG (Sittler,

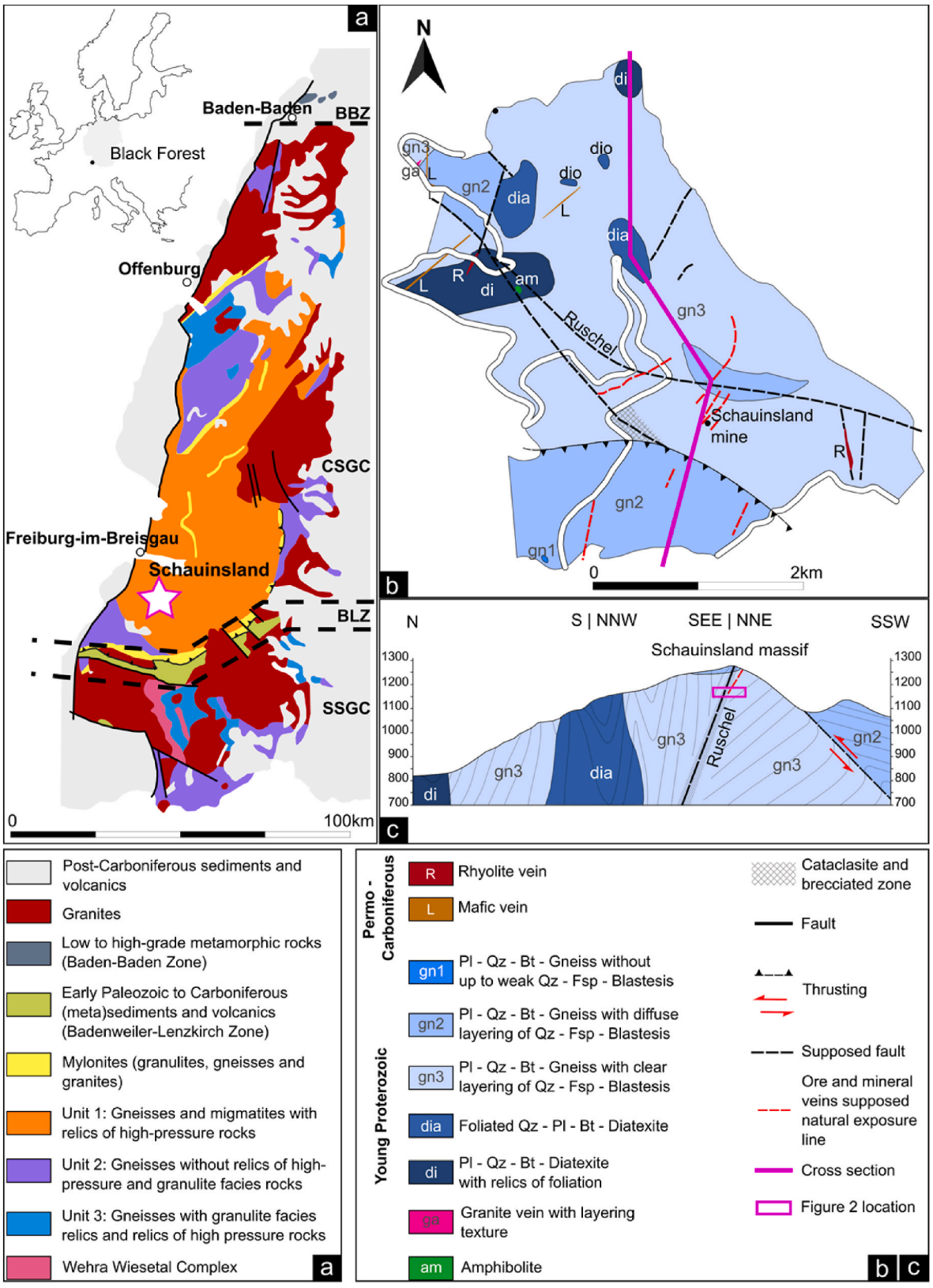

Fig. 1. (a) Simplified geological map of the southern Black Forest (modified after Altherr et al., 2019); (b) Geological map of the Schauinsland massif (modified after Wittenbrink, 1999); (c) N-S cross section of Schauinsland massif (modified after Wittenbrink, 1999). BBZ=Baden-Baden Zone, BLZ=Badenweiler-Lenzkirch Zone, CSGC=Central Schwarzwald Gneiss Complex, SSGC=Southern Schwarzwald Gneiss Complex. Bt = biotite, Fsp = Feldspar, Pl = Plagioclase, Qz = Quartz. Mineral abbreviations from Whitney et Evans 2010. (For interpretation of the references to colour in this figure legend, the reader is referred to the Web version of this article.)

1985). This was followed by the sedimentation of carbonates during the Jurassic. The area was uplifted and eroded from the Late Jurassic to the Early Eocene, leaving no evidence of Cretaceous sediments (Schumacher, 2002).

The initiation of the URG rifting started in the early Eocene under the north-oriented Alpine compression, reactivating ENE and NNE structures (Ziegler, 1992; Schumacher, 2002). At this stage, thermal anomalies and crustal thinning were described (Ziegler and Dèzes, 2005). The extension of the URG was West to WNW oriented from the Late Eocene to the Early Oligocene with the development of NNE faults (Schumacher, 2002). The late Oligocene SW compression reactivated the border fault of the URG with dextral shearing (Villemin and Bergerat, 1987; Schumacher, 2002). The Miocene recorded two compression events, beginning with a first NE-oriented event (Illies and Greiner, 1979; Bergerat, 1985; Edel et al., 2006) which transformed the URG into a shear zone followed by a NW compression related to the Alpine push and still today, reactivating North and NE faults (Rotstein and Schaming, 2011; Schumacher, 2002; Villemin and Bergerat, 1987).

The overall maximum horizontal stress of the URG is currently NW-oriented (Heidbach et al., 2016). However, there is a change in the faulting regime from the northern to the southern part of the URG (Meixner et al., 2016). The northern part is in an extensional setting and active normal faulting, the central part shows a transitional regime, while in the southern part of the graben strike-slip faulting prevails (Larroque et al., 1987; Cuenot et al., 2006; Meixner et al., 2014).

Overall, the URG still records seismic events with magnitudes ranging from 1.1 to 4.1, including natural and induced events (Doubre et al., 2022). Natural events show hypocenters at 10 km depth within the graben related to the reactivation of pre-existing structures and are more concentrated in the southern part of the URG. Induced events are associated with the reactivation of major faults within geothermal reservoirs during and after stimulation operations (Schmittbuhl et al., 2022). Moreover, the earthquake concentration is higher in the southern part of the URG where more earthquakes were recorded (Doubre et al., 2022).

On the South-eastern shoulder of the URG, the BF can be split into four tectono-metamorphic zones (Altherr et al., 2019) presented in Fig. 1a. The Baden-Baden Zone (BBZ), the Central Schwarzwald Gneiss Complex (CSGC), the Badenweiler-Lenzkirch Zone (BLZ) and the southern Schwarzwald Gneiss Complex (SSGC). The BBZ is composed of three tectonic slices, presenting various low-pressure and medium-temperature metamorphic rocks (Altherr et al., 2021). The CSGC comprises migmatitic paragneiss, orthogneiss, granodiorites, metabasites, peridotites, pyroxenites, granulites, and leucocratic gneisses with most of the protoliths of the metamorphic rocks being of Early-Paleozoic ages (Altherr et al., 2021). The BLZ (Krohe and Eisbacher, 1988) presents low-pressure and medium to very low-temperature metamorphosed tectonic units (Altherr et al., 2019). The SSGC is composed of four units of amphibolite facies rocks (Altherr et al., 2021). The metamorphism of the protolith took place along with the Variscan orogenesis (Geyer et al., 2011). Part of the BF is covered by Permian deposits (arkoses and conglomerates), Triassic quartzitic sandstones, limestones, shales, evaporites and clastic sediments and Jurassic carbonate and clastic sediments (Geyer et al., 2011).

Numerous types of mineralised veins highlight several hydrothermal events in the BF region which can be subdivided into five formation stages (Walter et al., 2016). For this study, we focus on the Jurassic-Cretaceous and Paleogene stages, which occurred at the same time as the studied fault zones in the Black Forest. The Jurassic-Cretaceous hydrothermal activity is associated with the opening of the Tethys and Atlantic rifts (Staude et al., 2009). Fluorite, carbonate, quartz and barite resulting from this event are related to a highly saline fluid circulation (Walter et al., 2016). Locally, a shear zone rich in clay minerals called the Ruschel fault zone (RFZ, Fig. 1b and c) was formed at that time. The Paleogene veins consisting of barite, quartz, fluorite and carbonates, and locally sphalerite and galena, result from the mixing of fluids from various aquifers (Walter et al., 2015).

The Black Forest is still seismically active with recent events in the CSGC at Waldkirch where magnitudes of 3.1 and 4.4 in 1979 and 2002 (Doubre et al., 2022) were recorded. Häge and Joswig (2009) showed a hypocenter alignment at 11 km depth with a WNW direction.

The BF Schauinsland massif (GPS: 47°54′42,82"N 7°53′54,65"E) and its mine galleries provide underground access to a 3D view of the geological structures. The host rock is mainly composed of paragneiss (Fig. 1b; Wittenbrink, 1999) that underwent several episodes of deformation since the Variscan orogeny. The RFZ is a WNW high-strain shear zone rich in clay which crosscuts the massif (Fig. 1c). It is approximately 35 m long and exposed in a NNE striking mine gallery (Fig. 2a) within the gneissic host rock (Fig. 2b). The RFZ shows an alternation between damage zones (DZ) and core zones (CZ) evidenced by vertical clayey gouge zones less than a meter wide, presenting a multi fault-core architecture. The largest clayey gouge zone is approximately 1 m wide. It was found in the centre of the RFZ and is interpreted as the main core zone (MCZ). In this study, the alternation between centimetre scale CZ and metric DZ towards the MCZ corresponds to the transition zone (TZ) of the RFZ as presented by (Choi et al., 2016).

The RFZ is dated from the Lower Jurassic to the Lower Cretaceous. Through its formation, the RFZ was reactivated multiple times and illitization processes occurred (Werner et al., 2002) which is observable by the highly dipping clay gouges (Fig. 2c) in the TZ. The RFZ was then cut and displaced by a NNE striking dextral transtensional fault zone from the late Oligocene to the Miocene (Rotstein and Schaming, 2011). Synkinematically, hydrothermal fluid flow brecciated the gneiss and resulted in an ore vein rich in quartz, sphalerite, galena, barite and carbonates (Werner et al., 2002). It is only visible on the roof of the gallery, except in the CZ of the RFZ, in the form of a hydraulic breccia (Fig. 2d).

The Schauinsland setting is considered an analogue to the fractured crystalline rocks used as geothermal reservoirs in the URG because the BF corresponds to a shoulder of the URG where kilometre-deep basement rocks in the graben are outcropping. The Variscan structural directions in the BF are the same as in the URG (NNE and WNW orientations). The main difference concerns the rocks that are gneiss in the BF and granite within the URG geothermal reservoirs. The two rock types have similar overall mineralogies. They also present deformation features such as local biotite foliation related to cooling deformation for the granite (Genter and Traineau, 1992) and a foliation for the gneiss. However, the gneiss foliation is also deformed and could induce anisotropy influencing potential preferential fluid pathways (Acosta and Violay, 2020). In this study, we focus on the tectonic setting and the interplay between the Schauinsland fault zones and not on the difference in mineralogy or microstructure between the granite and the gneiss.

The ore vein is considered an analogue of a tectonic structure setting in which occur present-day brine circulation within a fractured crystalline geothermal reservoir. The questions addressed in this study are: “How did the RFZ formed? How is the permeability distributed within a multi-core fault zone? What are the physical conditions under which migrating hydrothermal fluids can pass through a clay-rich fault zone?” A multiparameter characterization including petrophysical, petrographical, mineralogical and geochemical investigations have been performed along the gallery crosscutting the RFZ. Altogether, these data allow to reconstruct a geological history of the structure with its associated permeability distribution.

3. Materials and methods

3.1. Sampling and preparation for measurements

Forty hand-sized samples were collected along the mine gallery. They were taken at approximately 1 m away from the ore vein to have a constant influence of its formation on the samples. This allowed us to focus only on the effects of the RFZ on the gneiss (Fig. 2a). The sampling

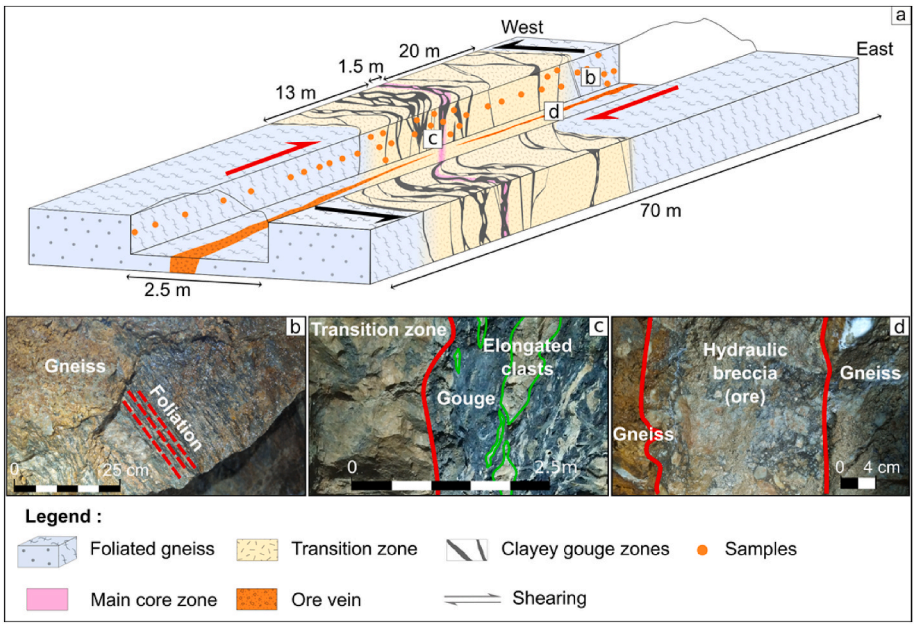

Fig. 2. (a) 3D conceptual geological scheme of Schauinsland gallery made from field observation. The Ruschel fault zone corresponds to the transition zone plus the main core zone. The older shearing is indicated by the dark arrows, the youngest one by the red arrows. Clayey gouge zones are exposed on the gallery walls. The outer plane of the gallery is represented with supposed projected geological features. The ore vein is represented in orange, disappearing close to the core zone. (b) Foliated gneiss. (c) Contact between a damage zone and the main core zone. (d) Ore vein constituted of a hydraulic breccia. (For interpretation of the references to colour in this figure legend, the reader is referred to the Web version of this article.)

interval is 5 m in the gneiss at a maximum and 3 m in the RFZ. However, if any lithological change was observed along the RFZ profile, additional samples were collected. The sample G32 corresponds to an ore vein sample and was collected on the roof of the gallery. One more sample, designated G1, was collected as far as possible from both the ore vein and the RFZ (respectively 3 and 46 m). The sample is considered the most pristine by being the farthest from the deformation and hydrothermal alteration of both the ore vein and RFZ formations. Thus, sample G1 is used as a reference to observe the evolution of hydrothermal alteration and deformation towards the RFZ. It was not possible to collect samples further away due to the mine geometry. Polished thin sections were prepared perpendicular to the foliation of the gneiss and parallel to the lineation when visible to crosscut all possible structural features for microscopic observations. The associated polished thick sections were used for elemental imaging using micro-X-ray fluorescence (μXRF). Fine powders were prepared using a tungsten carbide grinder for manocalcimetry, magnetic susceptibility and Diffuse Reflectance Infrared Fourier Transform spectroscopy (DRIFTS) measurements. Samples were dried at 50 °C for at least 24 h before using powders or rock samples for petrophysical or mineralogical investigation. If not specified, analyses were performed at the GEC laboratory in CY Cergy Paris Université (France).

3.2. Manocalcimetry

Manocalcimetry measurements were performed to quantify the carbonate content of the samples in weight percentage by using the OFITE 152-95 manocalcimeter, calibrated with pure calcite (Ledésert et al., 2009; Klee et al., 2021b). Hydrochloric acid with a 10% concentration was used to react with 1.000 g of sample powder. The dissolution of carbonates releases CO_2 that leads to a pressure increase in the calcimeter chamber (Eq. (1)). The calibration coefficient of the manocalcimeter and the measured maximum CO_2 pressure are used to calculate the carbonate content (Eq. (2)), with an uncertainty of 0.5 wt% (Ledésert et al., 2009).

$$CaCO_3\ (s) + 2HCl\ (l) = CO_2\ (g) + H_2O\ (l) + CaCl_2 \quad (1)$$

s = solid, l = liquid, g = gas

$$\%\ CaCO_3 = (A * 100) / C \quad (2)$$

Where A is the measured CO_2 pressure value and C the calibration coefficient of the instrument obtained using various amounts of pure calcite.

3.3. Porosity

The connected porosity of each sample was quantified using the triple weighing method to obtain the effective porosity measurement as done by Robion et al. (2014). The measurement was performed on three irregular rock fragments from each sample. The standard protocol for this method usually uses water to fill the pores of the samples, but in this study, ethanol was used instead to avoid swelling related to the presence of clay minerals (Bleam, 2012). Dried samples were weighed (m_1) and put under a vacuum for 18 h. Samples were then saturated with ethanol in the vacuum and weighed (m_2). Afterwards, saturated samples were immersed in an ethanol bath and weighed (m_3). The porosity values are obtained by using Eq. (3).

$$\Phi = (m_2\text{-}m_1 / m_2\text{-}m_3) *100 \quad (3)$$

3.4. Magnetic susceptibility

Magnetic susceptibility measurements were made 10 times for each sample using an AGICO KLY-4 Kappabridge by applying a constant field of 300 A/m (Meller et al., 2014). To obtain the mass susceptibility, the bulk values are normalized by the volumetric mass density of the sample (Eq. (4)). The volumetric mass density is evaluated from the mass used for the measurement within the known volume of the sample holder.

$$X = K / \rho \quad (4)$$

Where X is the mass susceptibiltiy in $m^3.kg^{-1}$, K the bulk susceptibility

in SI units and ρ the volumetric mass density of the measured powder in $kg.m^{-3}$.

3.5. Diffuse Reflectance Infrared Fourier Transform spectroscopy

The mineral composition of the samples was obtained by DRIFTS. This method is used for quick characterization of the sample powders (1:30 min per sample) and does not require any separation of the fine fraction to quantify clay minerals (Herron et al., 2014; Loan et al., 2017). These measurements were made at SLB SRPC GeoServices/Surface Logging Department, in Clamart (France) using a Bruker ALPHA II Compact FT-IR Spectrometer. Samples were analysed with a 4 cm^{-1} resolution in the infrared range from 375 to 4000 cm^{-1}. Spectrum intensities were measured in Kubelka-Munk units. The mean spectrum was obtained from 90 scans for each sample. Mineral phases identified with this method are chlorite, illite, kaolinite, smectite, muscovite, calcite, dolomite, anhydrite, as well as quartz and feldspar together. These phases were quantified in weight percentage with a standard deviation of less than 1%. No anhydrite signal was found in the whole mine except in the ore vein sample, hence, the given signal is interpreted as a sulphide rather than a sulphate signature.

3.6. Fracture density

The spatial arrangement of fractures in each sample was studied using QGIS version 3.10 software. Following the scanline procedure from Chabani et al. (2021) and Klee et al. (2021b), a straight line was drawn on a photograph of each polished thick section. The line crosses each sample and intersects the structures of the rock. Open fractures and veins intersecting the drawn line were marked. Their coordinates according to the scanline were recorded and used to quantify the fracture density P10 (Eq. (5); Gillespie et al., 1993). It is to be noted that, the P10 value only takes into account the number of fractures along the scanline and not their spacing.

$$P10 = n / L \quad (5)$$

Where n is the number of fractures and L the length of the scanline and P10 the fracture density.

3.7. Micro X-ray fluorescence

Element mapping was performed using a Bruker M4 Tornado micro-XRF instrument (De Winter and Claeys, 2017; Kaskes et al., 2021) at the AMGC laboratory in the Vrije Universiteit Brussel (Belgium). The instrument is equipped with a 30 W rhodium anode metal-ceramic X-ray tube and two 30 mm^2 silicon drift detectors. Measurements were made on the thick sections used for scanlines. Samples were placed in the instrument chamber under a 20 mbar vacuum. The X-ray source was set at 600 μA and 50 kV and no filter was used. Elemental maps are acquired with an integration time of 1 ms per pixel and a spatial resolution of 25 μm.

3.8. Principal component analysis

To understand the influence of each physical parameter on the others, a principal component analysis (PCA) was performed by using the FactoMineR package in R (Lê et al., 2008). PCA is commonly used to study the relationships between the different properties of samples resulting from various experiments.

4. Results

4.1. Structural overview

A structural map of the RFZ and the associated ore vein comprising foliation, clayey gouge zones, and fractures strikes and dips are presented in Fig. 3a. All the structural measurements are available as supplementary materials. The main foliation observed in the gneiss presents an overall NW striking with local variations along the gallery (Fig. 3b). Open and filled fractures within the gneiss and the transition zone present two main orientations. A NNE orientation that is parallel to the ore vein structure and another set of WNW fractures parallel to the overall orientation of the RFZ (Fig. 3a and b). Most of the fractures have dip values higher than 60° but some low dip angle fractures were also measured. Clayey gouge zones strike WNW and show an average dip of 76° (Fig. 3b). Nevertheless, a clayey gouge zone with a NNE strike is parallel with the ore vein. It highlights the ductile behaviour of the clay related to the ore vein shearing (Fig. 3b).

Moreover, a scanline perpendicular to the ore vein was performed (Fig. 3c) in a short corridor in the southern part of the gallery. 48 fractures were measured over the 4.2 m length of the scanline among which 29 fractures are filled with baryte. Open fractures are either NE or WNW oriented, which is close to the main orientations measured along the RFZ profile. At the opposite, filled fractures are mainly sub-verticals and NNE oriented with a striking value of N16°, similar to the ore vein (Fig. 3b). The scanline shows local fracture clusters marked by a frequency increase at 1.5, 2, 2.6, 2.7 and 2.9 m on the profile (Fig. 3c). Fracture spacing becomes more constant after 3 m. This likely suggests a limit to the ore vein influence on the fracturing of the gneiss.

4.2. Petrographical observations

Five samples representing the main rock lithologies along the RFZ profile are described in Fig. 4. The sample G1 is a quartz-rich gneiss characterised by a well-developed foliation and the occurrence of quartz veinlets (Fig. 4a). This lithology is found on the southern part of the gallery and remains consistent until the TZ of the RFZ (Fig. 3a). The sample L7 collected next to the MCZ is representative of the TZ. It shows a cataclasite with a whitish colour and the initial foliation is no longer distinguishable (Fig. 3b). Fractures and thin clayey gouge zones can be observed, indicating deformation and hydrothermal alteration events. Within the thin clayey gouge zones, altered gneiss clasts are observed, and present deformation features consistent with the WNW shearing direction. These clayey gouge zones display S-C structures resulting from the regional shearing (Rutter et al., 1986; Insua-Arévalo et al., 2021) and has a fractal aspect by containing smaller grains with the same structures. The MCZ is represented by the sample L8 which is matrix-supported thanks to abundant clay minerals (Fig. 4c). Lenses of hydrothermally altered and deformed gneiss remain within the clayey gouge zones. Brownish veins highlighting the deformation bands can be observed in the sample and result from the intense shearing of the MCZ. They follow the orientation of the RFZ. At a smaller scale, deformed gneiss lenses are observed (Fig. 4d). Their deformation follows the direction indicated by the deformation bands and highlights a ductile behaviour as for the clayey layers. On the northern part of the transition zone, the sample L6 shows similar features as the sample L7 except for the amount of clays which seems more abundant (Fig. 4e). Nevertheless, S-C structures are clearly observed in this sample. Thus, the transition zone lithology is composed of cataclasite incorporating thin clayey gouge zones resulting from the deformation and alteration of the gneiss. The gneiss sample G34 on the northern part of the gallery shows a deformed foliation locally crosscut by quartz veins (Fig. 4f).

4.3. Microscopical observations

The gneiss surrounding the RFZ is mostly composed of quartz, plagioclase, and biotite with a grain size ranging from 0.1 to 1 mm (Fig. 5a, Table 1). The foliation is given by the preferential orientation of the biotite and can be crosscut by quartz or calcite veins of up to 2 mm width (Fig. 5b). Biotite shows evidence of slight hydrothermal alteration leading to partial replacement by illite (Fig. 5c). Biotite-rich layers show

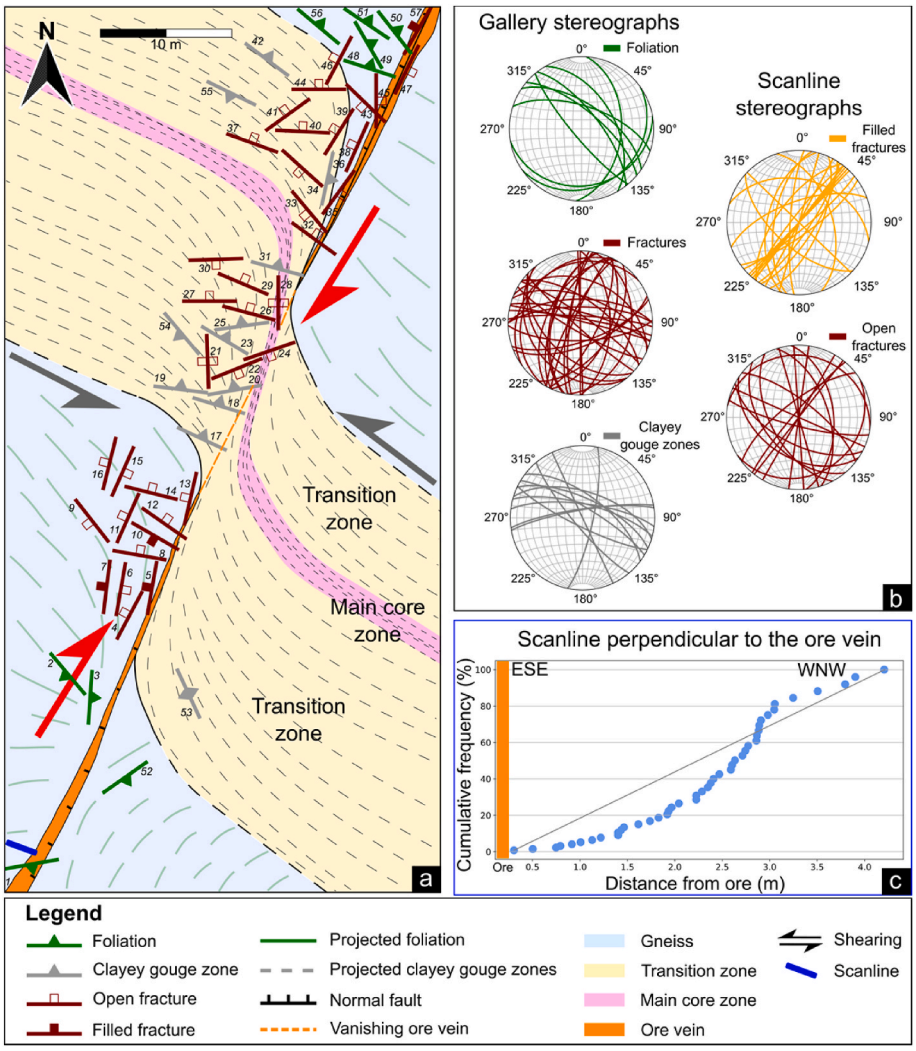

Fig. 3. Structural measurements of open and filled fractures, clayey gouge zones and foliations along the gallery and perpendicular to the ore vein. Measurements done by Werner et al. (2002) are represented in the figures and all values can be found in the supplementary data. (a) Structural map of the Ruschel fault zone and the perpendicular ore vein. The transition zone and the main core zone are respectively in yellow and pink. The gneiss and the ore vein are in blue and orange. The first shearing associated with the RFZ is represented by the dark arrows while the later one associated with the ore vein formation is in red. A scanline perpendicular to the ore vein indicated by a red line was done as far as possible from the RFZ, in a short perpendicular corridor. Measured planar discontinuities are numbered and their data are accessible as complementary material. (b) Schmidt lower hemisphere stereograph of measured planar discontinuities in the gallery and along the scanline. (c) WNW oriented 5 m-long scanline perpendicular to the ore vein. Each fracture encountered along the profile is represented by a dot on the plot. The scanline shows the cumulated fracture frequency distribution along its profile. (For interpretation of the references to colour in this figure legend, the reader is referred to the Web version of this article.)

an increase in the hydrothermal alteration degree compared to the gneiss G1, and tend to localise the deformation (Fig. 5d). These layers are enriched in clay minerals and create deformation bands and lenses highlighting the direction of deformation (Fig. 5d).

Within the TZ, the lithology evolves to a cataclasite comprising milimetre-scale clayey gouge zones. Mineral transformations within plagioclase crystals are highlighted by the presence of calcite (Fig. 5e). Thin calcite fault-veins with a maximum width of 0.2 mm and a blocky aspect are found in the whole thin section and are more numerous compared to the veins observed in the gneiss (Fig. 5f). Biotite and plagioclase crystals are less abundant than in the gneiss as they are more hydrothermally altered and replaced by secondary phases such as calcite or clay minerals (Fig. 5e and f; Table 1). Moreover, within the TZ, finer grain size is observed compared to the gneiss and grains of 0.04 mm width are observed. This is accompanied by an increase in the fracture density observed at the milimetre-scale either in the quartz or plagioclase minerals resulting from their grain size reduction indicating a brittle behaviour.

Clay-rich gouges are scarce in the TZ and they mainly compose the MCZ of the RFZ (Fig. 5g and h). Gouges present the highest hydrothermal alteration and deformation degree. Primary phases such as biotite and plagioclase are replaced by clay minerals or carbonate (Table 1). The grain size of the clayey matrix is smaller than 1 μm. It can no longer be quantified using optical microscopy compared to the gneiss and the cataclasite. Rounded quartz grains and preserved deformed quartz lenses with a size reaching 1 milimetre surrounded by brownish veins of up to 0.4 milimetres in width are contained within the clayey matrix (Fig. 5g and h). The brownish veins correspond to the deformation bands described in Fig. 4c and present a mix of carbonate and iron oxide. Calcite veins and patches can still be found in the matrix. Most of the plagioclase and biotite crystals are fully transformed into secondary minerals and only small relicts of the primary remain observable.

4.4. Petrophysical properties

To better represent the evolution of the petrophysical and

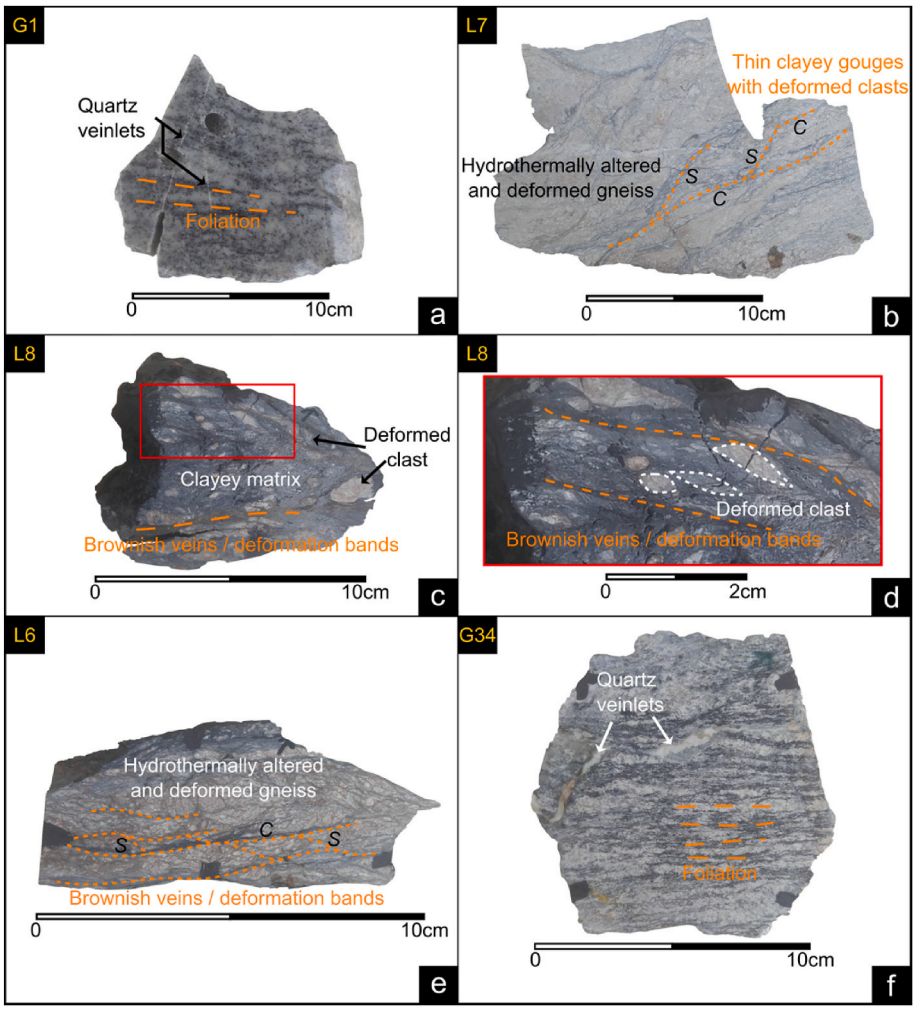

Fig. 4. Handsize polished sections of 5 samples representing the main lithologies observed along the gallery. (a) Gneiss sample G1 from the southern part of the gallery, its foliation is underlined in orange and the sample is crosscut by some veinlets. (b) Cataclasite sample L7 from the transition zone of the RFZ. The foliation is no longer observable on the sample. The gneiss is hydrothermally altered and deformed. Some thin clayey gouge zones comprising deformed clasts crosscut the sample and highlight C and S structures. (c) Clay-rich gouge sample L8 from the main core zone of the RFZ. The sample is highly enriched in clay minerals and contains deformed clasts. Brownish veins related to the shearing of the sample underline deformation bands in orange. (d) Zoom on the L8 sample. Deformed clasts show evidence of ductile behaviour within the clayey matrix. (e) Cataclasite sample L6 from the transition zone of the RFZ is composed of hydrothermally altered and deformed gneiss. The sample is crosscut by brownish veins underlining S-C structures and deformation bands. (f) Gneiss sample from the northern part of the gallery. Some veinlets are parallel to or crosscut the foliation which is underlined in orange. (For interpretation of the references to colour in this figure legend, the reader is referred to the Web version of this article.)

mineralogical properties of the samples, their positions are indicated on a geological sketch of the gallery with the principal lithologies (Fig. 6a). The ore vein presented in Fig. 2d is only visible on the roof of the gallery and thus is not represented in Fig. 6a. Its associated sample, G32, is compared to the other samples.

Magnetic susceptibility values are presented in Fig. 6b. Despite a certain dispersion, the magnetic susceptibility values seem to increase towards the MCZ, even though the range of values is narrow (e.g. $0.85e^{-8}$ for G1 and $2.90e^{-8}$ for L8 samples), consistent with a paramagnetic signature.

The porosity data in Fig. 6c show low values in the gneiss that increase towards the MCZ. The porosity of the gneiss is lower than 2.5% with a lowest value of 0.42% which is common for crystalline rocks. It increases within the TZ and reaches mean values of 5.9% and 4.6% in the southern and northern parts of the gallery. The MCZ sample has the highest porosity value of 13.1%.

Fracture density data represented by P10 values are shown in Fig. 6d. The gneiss always has values lower than 5 fractures/centimetre. The TZ is characterised by an increase in P10 values with average values of 12.1 and 9.4 fractures/centimetre on the southern and northern parts respectively. The MCZ reaches a value of 19.8 fractures/centimetre. This increase can also be observed on thin sections (Fig. 5f and g) where minerals exhibit more fractures. Local increased values are observed in the TZ for samples G17, L6 and G25 (16.5, 26.3 and 12.2 fractures/centimetre).

4.5. Mineralogical content

Fig. 6e summarizes carbonate content values obtained using manocalcimetry. Three different zones correlated with the lithological features are again distinguished. The gneiss shows a mean carbonate content of around 3.8% in the southern part and 4.8% in the northern part. Conversely, the TZ is characterized by an overall mean content of 9.1%. Locally, higher values are observed within the TZ in the case of samples G17 and G27 (11.5% and 13.0%). The highest carbonate content is found next to the MCZ with a value of 15.6%.

DRIFTS mineralogy data are shown in Fig. 6f. The clay content (illite, chlorite, smectite and kaolinite) of the gneiss is around 30%. The

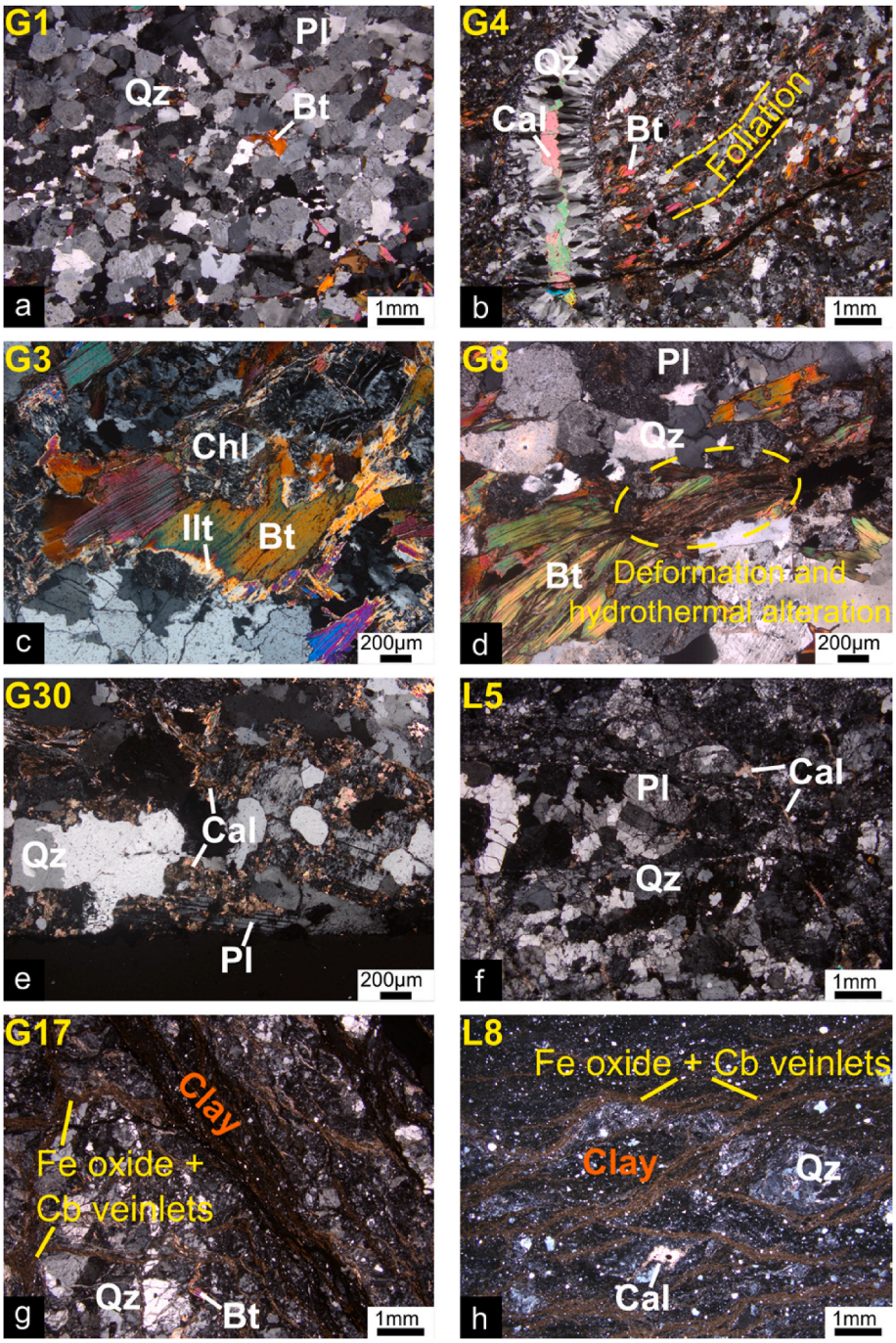

Fig. 5. Thin sections microphotographs (cross-polarized light). The sample designation is marked on each image in yellow. (a) Gneiss assemblage in the Schauinsland gallery. (b) Foliation of the gneiss underlined by biotite crystals. Crosscutting quartz and calcite vein. (c) Localized chlorite and illitized biotite in the gneiss. (d) Deformation bands with altered biotite layers. (e) Hydrothermal alteration of plagioclase partly replaced by calcite precipitation. (f) Gneiss with smaller grain size, mineral crushing, calcite veins and increased fracture density. (g) Clay-rich gouge with a very small grain size surrounded by highly fractured and hydrothermally altered minerals. Brownish veins filled with carbonate and iron-bearing minerals in clay-rich area. (h) Dark gouge with fine grained clayey matrix containing remains of fractured and deformed quartz grains. Local mineralisation of calcite. High concentration of brownish veins surrounding lenses of quartz. Qz = quartz, Pl = plagioclases, Bt = biotite, Cal = calcite, Ilt = illite, Chl = chlorite. Mineral abbreviations from Whitney and Evans, 2010. (For interpretation of the references to colour in this figure legend, the reader is referred to the Web version of this article.)

Table 1
Modes of the gneiss, cataclasite and clayey gouge zone observed through the RFZ. The composition is estimated from thin section analyses with an uncertainty of ±5%.

Lithology	Quartz (%)	Plagioclase (%)	Biotite (%)	Calcite (%)	Clay (%)	Iron oxide + carbonate (%)
Gneiss	45	40	10	<2	5	0
Cataclasite	40	25	<5	15	20	0
Clayey gouge zone	10	<1	<1	5	70	15

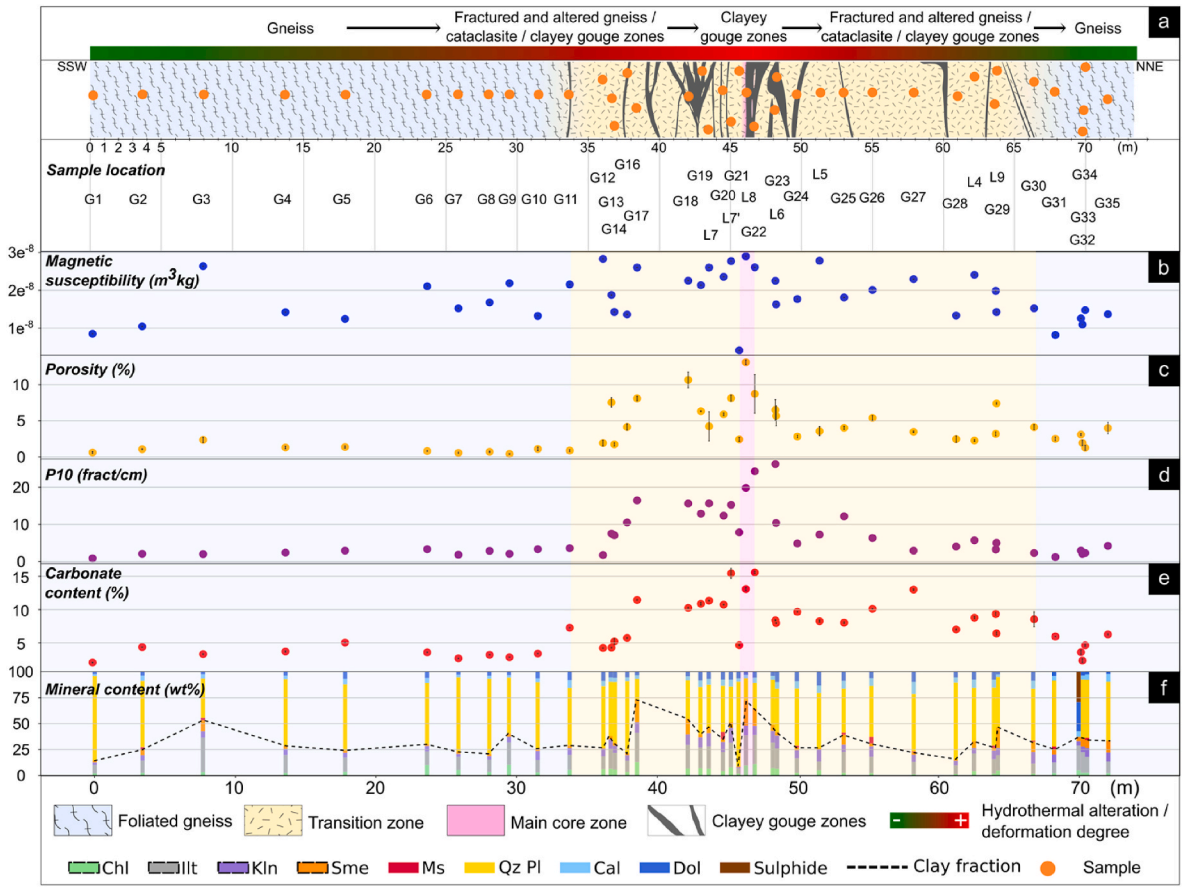

Fig. 6. Synthesis of all petrophysical and mineralogical data on 44 samples. (a) Geological conceptual schematic of the studied gallery wall with the position of each sample. The change in colour shows the different parts of the fault zone (light blue: gneiss, yellow: damage zone and light pink: core zone). Clayey gouge zones crosscut the gallery wall in the damage and core zone and were used as limits for these domains. The deformation and alteration degrees are represented by the horizontal-coloured bar at the top of the section. (b) Magnetic susceptibility measurements obtained with the kappabridge. instrument (c) Porosity measurements from triple weighing with ethanol method. (d) Fracture density (P10) obtained on thick sections at the centimetre scale (e) Carbonate content values measured with the manocalcimeter (f) Diffuse reflectance infrared Fourier transform spectroscopy (DRIFTS) measurements presenting the mineralogical evolution along the profile. (For interpretation of the references to colour in this figure legend, the reader is referred to the Web version of this article.)

southern and northern parts of the TZ have mean values of 40.2% and 35.3%. Within the MCZ, the clay content reaches 72.6%. However, some samples outside the MCZ also contain high concentrations of clays such as G17 (73.4%) and G18 (55.1%). These local variations are characterised by a major increase in smectite and illite contents. The quartz and feldspar content decreases with increasing clay content. The lowest values occur in the MCZ and the highest ones in the gneiss. Some exceptions to this general trend can be observed. Sample G21, next to the MCZ, indicates a high quartz and feldspar content (81.6%) due to the occurrence of a quartz vein. Calcite and dolomite contents obtained with the DRIFTS show higher values compared to the manocalcimetry. High calcite and dolomite content still occur in the TZ in G27 and L5 (21.3% and 20.5%). The sample G32 shows a high sulphide content (29.2%) mostly corresponding to galena because it was collected from the ore

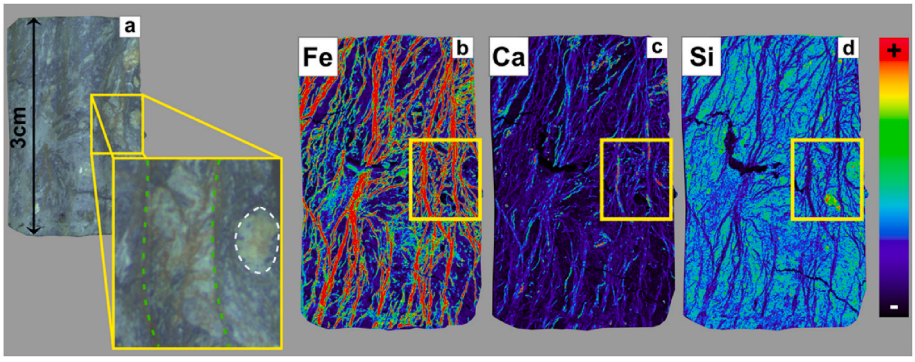

Fig. 7. Micro XRF element maps of the thick section of sample L8 from the core zone. The Ca, Fe, Si micro XRF heat maps provide an overview of the relative content of an element from black (low) to red (high). The yellow rectangle on the elemental maps corresponds to the one on the microphotograph. (a) Microphotograph of the sample with a zoom (delimited by the yellow rectangle) on Fe rich veins and Si rich grains are underlined in green and white. (b, c and d) Heat maps of the Fe, Ca and Si concentrations respectively. (For interpretation of the references to colour in this figure legend, the reader is referred to the Web version of this article.)

vein. Its mineralogical composition also differs from the rest of the samples as it does not contain any trace of quartz and feldspar. It has the highest content of calcite and dolomite (33.6%), but cannot be compared to the other samples made of gneiss and associated transformation products.

4.6. Element mapping

Element maps of Fe, Ca and Si showing the relative concentration of these elements in the thick sections of sample L8 collected in the MCZ are shown in Fig. 7. A dark matrix with brown veins and whitish rounded grains is observed on the microphotograph of the sample (Fig. 7a). Iron mapping shows a high concentration within the brown veins (Fig. 7b). Calcium is locally present in the sample and tends to be concentrated along the Fe-rich veins (Fig. 7c). However, the matrix has a low Ca concentration. The Si content is overall low in the sample, especially in the Fe-rich vein network (Fig. 7d). Remnants of the gneiss in the matrix exhibit an overall higher Si concentration.

4.7. Statistical characterisation

PCA using dimensions 1, 2 & 3 is presented in Fig. 8. These 3 dimensions represent 73.1% of the data information. They consider the magnetic susceptibility, porosity, carbonate content, fracture density and mineral contents that are depicted in Fig. 6. The ore vein sample G32 is discarded because of its composition that might alter the results and geological interpretations due to the sensitivity of the PCA to extreme values (Fig. 6f).

Similar directions of vectors indicate that the concerned variables are well correlated. This is the case for the vectors representing the variables muscovite, calcite and dolomite in the graph of dimensions 1 and 2 and for the illite, chlorite and smectite vectors that are close to one another and point towards the same direction. The quartz with feldspar content is negatively correlated with all the other variables except in the case of muscovite, dolomite and calcite (Fig. 8a). The magnetic susceptibility vector falls between the kaolinite, carbonates and the porosity vectors. The porosity vector direction lies between those of illite and magnetic susceptibility and is strongly correlated with the fracture density (P10; Fig. 8a).

With dimensions 1 and 3, the variable quartz and feldspar is negatively correlated to all the variables except for the dolomite and muscovite (Fig. 8b). The calcite and smectite are highly correlated. P10 is bordered by the magnetic susceptibility and kaolinite content. There is a correlation between the porosity, illite and carbonate contents (Fig. 8b).

5. Discussion

5.1. Deformation and alteration processes in a high-strain shear zone

5.1.1. Deformation

Deformation evidence, such as grain size reduction, fracturing, and cataclasis in the RFZ, are used to characterise the deformation distribution in a multi-core fault zone and its permeability (Caine and Tomusiak, 2003; Torabi et al., 2020). Crystalline rock fracturing leads to an increase in permeability after any fault activation event (Sibson, 1992; Caine and Tomusiak, 2003). As shown by Bertrand et al. (2021), the fracture density and porosity in crystalline rocks increase towards a fault core zone. This relationship is observed in the RFZ (Fig. 6c and d) and shows an increase in the deformation degree towards the MCZ with local variations in the TZ already described by several authors (e.g. Caine et al., 1996; Faulkner et al., 2010; Choi et al., 2016). This suggests a potential permeability increase in the most deformed structures such as cataclasites or clayey gouge zones. From the measured porosity and fracture density values, local increases are observed along the RFZ (Fig. 6c and d). Thus, this can be assimilated with the presence of the clayey gouge zones distributed along the RFZ profile which would indicate previously permeable fractures. As the prevailing porosity might be related to the fractures, the formation of the RFZ would have enhanced the porosity and therefore the permeability of the structure (Caine and Tomusiak, 2003).

The distribution of these fractures and their associated permeabilities in the RFZ is also dependent on their orientations and the presence of pre-existing structures. As demonstrated by Torabi et al. (2020), higher fracture permeabilities are expected for features parallel to fault structures and not perpendicular. During the formation of the RFZ, its structural orientation is WNW (Fig. 3a). Fractures with similar orientations are expected to be favourable pathways for fluid flow as shown by the orientation of the clayey gouge zones (Fig. 3b). Moreover, structural inheritance also affects the deformation distribution as pre-existing structures tend to concentrate the deformation during the early development of a fault zone (Schumacher, 2002; Callahan et al., 2020). It implies that the formation of later permeable structures might be found next to pre-existing features. Indeed, the Variscan Badenweiler-Lenzkirch zone in the Black Forest (Krohe et Eisbacher, 1988) presents a similar orientation to the RFZ and it is likely that it has been reactivated through its formation.

At the sample scale, a grain size reduction (Fig. 5f and g) as well as an increase in mineral fracturing (Fig. 6d) are observed in the TZ, compared to the reference gneiss. Cataclasites presenting deformation bands and S-C structures are observed and show evidence of shearing in the RFZ (Fig. 4b–e). Within the clayey gouge zones, deformed and rounded clasts which are hydrothermally altered are found (Fig. 5g and h). Such grains

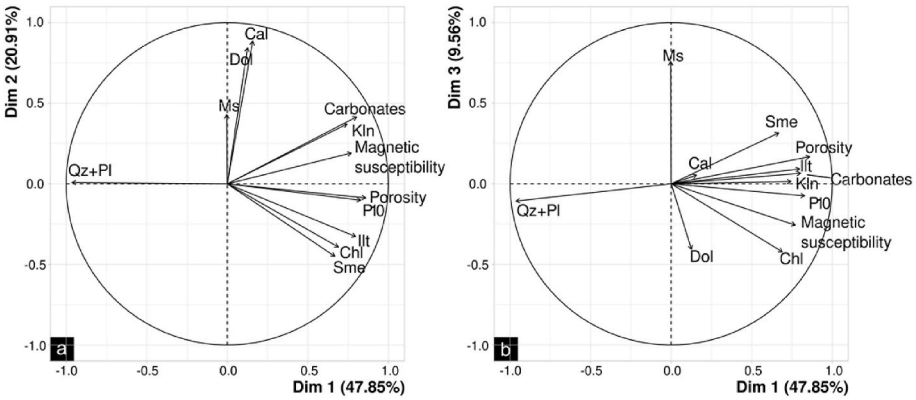

Fig. 8. Principal component analysis of the petrophysical and mineralogical measurements using magnetic susceptibility, porosity, carbonate content, fracture density, and DRIFTS mineralogical records. (a) Variable analysis for dimensions 1 and 2. (b) Variable analysis for dimensions 1 and 3. P10 = fracture density, Mag sus = magnetic susceptibility, mineral abbreviations from Whitney et Evans 2010.

might result from the cataclastic flow of the minerals through the shearing of the RFZ. Moreover, quartz lenses found in these gouges (Fig. 5h) are similar to the lenses described by Torabi et al. (2020) within slip surfaces of gneissic shear zones. The quartz lenses seem to have accommodated most of the deformation while the phyllosilicates show evidence of smearing under the RFZ shearing. This is consistent with similar lab results obtained by Bedford et al. (2022). Such a mix of materials with low and high friction coefficients (Wibberley et al., 2008) implies that the distribution of the deformation during the shearing cannot be predicted precisely. Indeed, each slip surface might have a different mechanical response to a shearing episode related to the amount of quartz and clay in the rock.

5.1.2. Evidence of fluid circulation

Evidence for fluid circulation and associated fluid/rock interactions such as primary mineral hydrothermal alteration and quartz, calcite and phyllosilicate precipitations, are observed across the RFZ and affect both the multi-core fault zone permeability and mechanical properties. The permeability of crystalline rocks is generally governed by the presence of fractures and can be affected by fluid flow (Faulkner et al., 2010). Fluid discharge in the fracture network is at its highest immediately after any rupture event through the seismic cycle of a fault zone (Sibson, 1992) and initiates fluid/rock interactions.

The hydrothermal alteration of primary phases is observed in the TZ with the transformation of plagioclase crystals (Fig. 5e) and hydrothermally altered biotite in the gneiss (Fig. 5d). This is also seen in the clayey gouge zones which present a Si depletion where only relicts of the gneiss are enriched in Si compared to the clayey matrix (Fig. 7d). These observations match with the measured decrease in quartz and feldspar towards the MCZ from DRIFTS analysis (Fig. 6f.) Such transformation phenomenon might have increased the permeability and weakened the RFZ especially towards the MCZ where the hydrothermal alteration is at its highest.

However, the precipitation of secondary phases was found in both gneiss and RFZ. Quartz and carbonate veins were found within the gneiss (Fig. 5b), suggesting the circulation of Si and Ca-rich fluids. Carbonate precipitation within fractures and clayey gouge zones in the RFZ are more abundant than in the gneiss (Fig. 5f–h). These precipitations also fill the space resulting from plagioclase hydrothermal alteration (Fig. 5e). The circulation of highly saline fluid in the Jurassic-Cretaceous time (Walter et al., 2016) within the fracture network could have led to the precipitation of these phases. Thus, the TZ would be the preferential volume of the fault structure for fluid flow as suggested by Meller and Ledésert. (2017) in Soultz's granitic geothermal reservoir.

Another evidence of fluid circulation and secondary phases are the brownish veins in the clayey gouge zones which are a mix of carbonate and Fe (Fig. 5g and h and Fig. 7b). These veins seem to display a dendritic network following deformation bands similar to Duwiquet et al. (2021) observations in granites which they interpreted as paleo-fluid flow traces. The iron mineralisation might be related to the Fe leaching, from the biotite in the gneiss (Fig. 5c and d). Walter et al. (2019) already described such a process in the area.

Clay minerals are abundant throughout the RFZ and serve as evidence of hydrothermal alteration and fluid flow. From the DRIFTS results, the clay phases resulting from hydrothermal alteration are illite, chlorite, smectite and kaolinite (Fig. 6f). Illite and smectite are the predominant phases within the gouges, which are the most hydrothermally altered structures of the RFZ. Nevertheless, the clayey gouge zones distribution is not homogeneous along the RFZ with local increases observed in the TZ (Fig. 6f). Dezayes et al. (2021) worked on a granite body located in the Vosges, on the western shoulder of the URG. They depicted the formation of illite/smectite mixed clay minerals linked with the alteration of the biotite, which is similar to the hydrothermal alteration processes observed in Schauinsland gneiss (Fig. 5c) where clay minerals compose the rock matrix of the gouges (Fig. 5g and h). The presence of both clays, quartz and carbonate precipitation is observed in the RFZ and clearly in the MCZ. It suggests an increase in the hydrothermal alteration degree towards the MCZ with local variations in the TZ which is consistent with the observations of Glaas et al. (2021), Sutherland et al. (2012) and Klee et al. (2021b). Thus, these observations would indicate favourable conditions for a fluid flow that promoted the crystallization of clay minerals (Inoue, 1995; Glaas et al., 2021) in previously permeable structures before clogging. Meller and Kohl. (2014) also showed that the magnetic susceptibility of the Soultz granite collected from the geothermal drill holes can be related to the clay content and as such, to the degree of hydrothermal alteration that allows the detection of fluid flow pathways. At Schauinsland, the magnetic susceptibility data tend to slightly increase towards the CZ. However, the range of values is not large enough to observe significant differences between the different parts of the RFZ (Fig. 6b).

The heterogeneous distribution of the clayey gouge zones with the quartz and carbonate precipitations could affect the mechanical behaviour of the RFZ. Clays with a low friction coefficient could have weakened the structure while quartz and carbonate would have strengthened the fractures. This could have led to different mechanical response of the RFZ through its seismic cycle with different responses to the shearing (Callahan et al., 2020).

5.2. Geological history of the ore-shear zone complex structure

The complexity of the structure with the interaction between two fault zones relies on various geological processes which have occurred since the Variscan orogenesis and have been recorded in the basement (Altherr et al., 2021). The present interpretation of the structure (Fig. 9) is based on pre-existing structures that localised subsequent deformation and alteration processes (Schumacher, 2002; Wibberley et al., 2008; Chauvet, 2019; Glaas et al., 2021; Klee et al., 2021b) and previous descriptions and interpretations by Werner et al. (2002).

5.2.1. Variscan inheritance of the permian basement

The Variscan orogenesis deformed and fractured the basement of the BF (Geyer et al., 2011), creating East and NNE-oriented structures (Fig. 9a) during the Permian (Schumacher, 2002), due to the Badenweiler-Lenzkirch shear zone (Krohe and Eisbacher, 1988) and dyke intrusions (Werner et al., 2002). At this stage, the permeability of the gneiss was fracture-controlled.

5.2.2. Start of shearing during the Lower Jurassic

A first East-oriented shearing episode occurred at the Lower Jurassic (Werner et al., 2002) reactivating Variscan structures with the same orientation (the Badenweiler-Lenzkirch shear zone) and acting as weakness features. This episode led to cataclasis, grain size reduction and development of secondary fractures generating an initial DZ around the FC (Fig. 9b) of the RFZ. At this stage, we consider that the RFZ had a single-core architecture. This process increased the overall porosity (Fig. 6b) and permeability of the RFZ (Fig. 6d; Caine and Tomuziak, 2003). After the first shearing, during the postseismic phase of the RFZ (Sibson, 1992), the CZ became the most permeable part of the structure, and the associated circulation of brines from the Triassic-Jurassic sedimentary cover and from the metamorphic basement (Walter et al., 2015, 2016) initiated the hydrothermal alteration of the gneiss and the precipitation of secondary phases (Fig. 9c).

5.2.3. Shifts from conduit to barrier behaviour until the Lower Cretaceous

According to Werner et al. (2002), the shearing activity lasted until the end of the lower Cretaceous. The PCA underlines a positive correlation between the porosity and fracture density (Fig. 8a) along with a positive correlation between the porosity with the clay minerals and carbonate content (Fig. 8b). This implies that through the formation of the RFZ, the shearing induced fractures increased the porosity, permeability and fluid/rock interactions ratio (Fig. 6d and e). During the multiple seismic cycles of the RFZ, fluid released in the fracture network

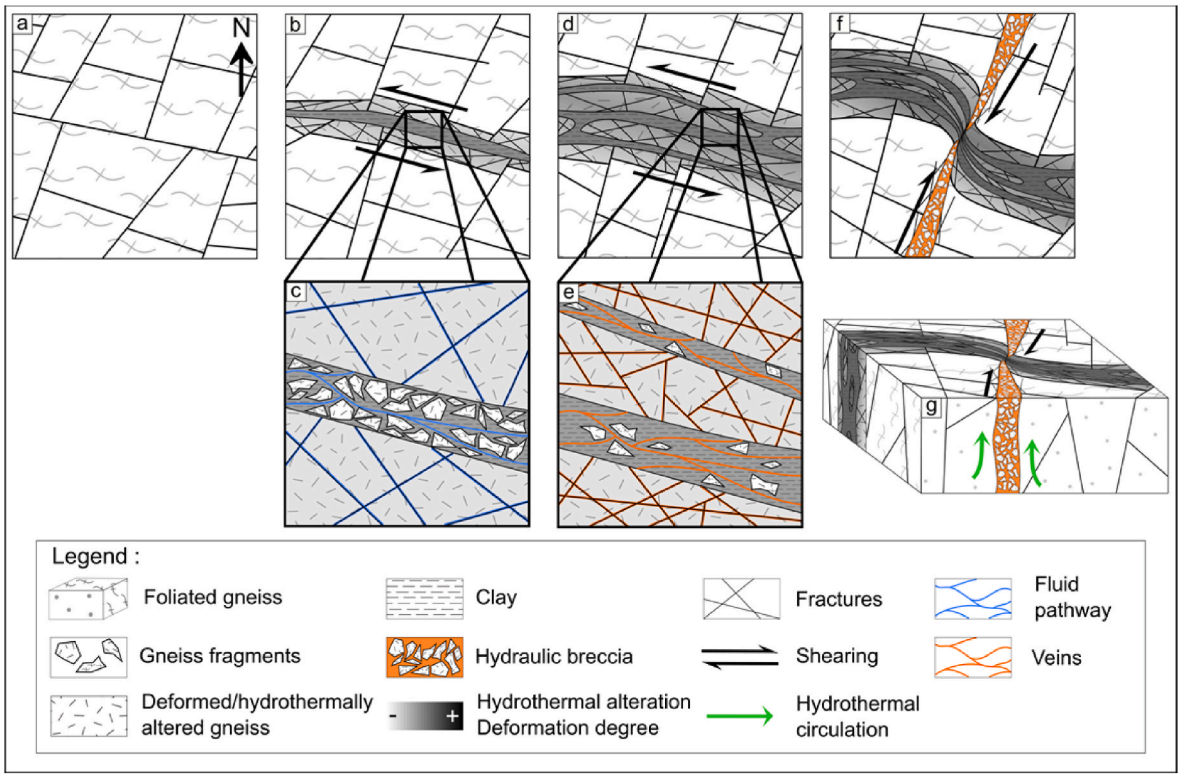

Fig. 9. Conceptual schematic drawing of the tectonic evolution leading to the formation of the Schauinsland complex structure: map view (a to e) and 3D block (g). (a) Variscan inheritance of the Permian basement. (b) Start of the shearing at the Lower Jurassic. (c) Zoom on the fault core formation during the Lower Jurassic where fluids are circulating. (d) Multi-core fault architecture resulting from the repetition of shearing episodes coupled with fluid flow until the Lower Cretaceous. (e) Zoom on the core zones with the precipitation of minerals that clogged the system after the last shearing episode of the Lower Cretaceous. (f) Dextral transtension during the Cenozoic, perpendicular to the Variscan structure. (g) 3D view of the structure during the Cenozoic. (For interpretation of the references to colour in this figure legend, the reader is referred to the Web version of this article.)

after rupturing generated hydrothermal alteration of primary minerals and precipitation of secondary phases which impacted the permeability and mechanical properties of the RFZ (Caine et al., 1996; Faulkner et al., 2010; Bense et al., 2013; Callahan et al., 2019). The permeability of the CZ shifted from a conduit to a barrier (Bense et al., 2013; Callahan et al., 2020) as represented in Figs. 5h and 9d. This shift is due to the high amount of clay minerals, quartz, carbonate, and grain crushing in the CZ that clogged the porosity.

With the permeability destruction and precipitation of secondary phases, the RFZ could have accommodated new shear stresses and reactivated already sheared structures through its seismic cycle (Sibson, 1992).

The clayey gouge zones, porosity, fracture density and clay content do not present a continuous trend along the section (Fig. 6c, d, f) and are evidence of the multi-fault core architecture of the RFZ (Wibberley and Shimamoto, 2003; Faulkner et al., 2010; Savage and Brodsky, 2011; Bischoff et al., 2024). The thin section of the G17 sample in the TZ shows the same feature as in the MCZ with the L8 sample but on a more local scale (Fig. 5g and h). Samples G17, G18, G22 and L9 in the TZ also have mineralogical compositions close to those in the MCZ, characterized by a major increase in smectite and illite (Fig. 6f). Some samples in the TZ also display high porosity and fracture density values along the profile, compared to neighbouring samples (Fig. 6c and d). Such heterogeneity could result from the widening of the RFZ through the repetition of the seismic cycle until the Lower Cretaceous leading to the fault-valve behaviour described in (Sibson, 1992, 2007).

However, the RFZ mixes clay minerals with a low friction coefficient and quartz and carbonate with a high friction coefficient. They affect the mechanical behaviour of a fault zone in different ways. The RFZ widening could result from two mechanisms. The MCZ could have been strengthened by calcite and quartz precipitation, leading to its widening through shearing (Callahan et al., 2020). Clay formation associated with fluid flow within the RFZ might have weakened the structure. This stopped the stress accumulation (Meller and Kohl, 2014; Schuck et al., 2020), leading to reactivation of surrounding fractures in the TZ and smearing of the clayey gouge zones (Fig. 7d). This is observed by the sample's properties, the lenses of preserved gneiss and the vertical gouges (Fig. 2c).

The mineralisation of the dendritic Fe-rich veins (Fig. 5g and h and Fig. 9e) and the Si depletion within the CZ could indicate a clogging of the remaining porosity resulting from the fluid/rock interactions (Fig. 7d), which would be the last episode of fluid circulation.

5.2.4. *Transtension and hydraulic brecciation during the cenozoic*

The Cenozoic corresponds to the opening of the ECRIS, including the URG (Ziegler, 1992). A dextral transtensional shearing parallel to the border faults of the graben affected the RFZ in a perpendicular NNE direction (Werner et al., 2002, Fig. 9f). The reactivated North oriented structures from the Variscan formed the main channels of this latest hydrothermal fluid circulation (Pfaff et al., 2009). The formation of the hydraulic breccia containing the ore vein rich in galena and sphalerite, resulted from this event. Since the RFZ is WNW-oriented, it is not considered preferentially oriented for reactivation. Thus, due to the high clay content of the MCZ and its impervious behaviour, the RFZ could not have been reactivated and was a barrier to the ore vein formation. A major feature of the ore vein is that it vanishes close to the MCZ of the RFZ and reappears on the other side of the structure (Fig. 2a). This feature might be related to differential mechanical behaviour between the gneiss and the RFZ, especially within the MCZ clays, which smear under shearing (Bedford et al., 2022). Several authors (Walter et al.,

2015, 2016; Vidal and Genter, 2018; Bossennec et al., 2021; Dezayes et al., 2021) presented hydrothermal systems in the URG where deep brines rise along major fractures. In the present context, the gneiss would have been fractured, while the MCZ only smeared. This fracturing coupled with high fluid pressure from underground, could have created ascending pathways on both sides of the RFZ, leading to the present ore vein (Fig. 9g).

5.3. Impact on current-day permeability

Using this complex structure as an analogue for the geothermal reservoirs of the URG provides an opportunity to identify highly permeable structures in fault zones and understand how brines interact with clay-rich shear zones. The Schauinsland setting, similar to the URG geothermal reservoirs, presents an intra-basement fault similar to the Rittershoffen geothermal site and interactions between fault zones as observed in the Illkirch geothermal project (Glaas et al., 2021), where a targeted NNE fault is not naturally permeable. Moreover, most of the permeability in the Illkirch basement is associated with fractures oriented N149°E and dipping 86°E and W, where the vertical alternation between different degrees of hydrothermal alteration and mineral filling was described between the permeable fractures (Glaas et al., 2020), comparable to the multi-fault core setting of the RFZ.

The increase in porosity towards the MCZ might suggest an increase in permeability (Klee et al., 2021b), but the whole TZ is crosscut by several clayey gouge zones considered to act as a barrier for fluid flow due to their clay content (Ledésert et al., 1999). Areas with higher hydrothermal alteration indicate prior fluid circulation events (Vidal and Genter, 2018; Glaas et al., 2021), and thus potential fluid pathways that could be reactivated with stimulation techniques. Samples in the TZ with a high fracture porosity, a large amount of carbonate, and clay traces would be the preferential locations for fluid flow. The presence of quartz or carbonate veins also correspond to fractures where fluids have circulated.

However, the multi-core zone architecture of the RFZ might compartmentalise the permeable parts of the TZ, as they are crosscut by the clayey gouge zones. Consequently, the permeability across the RFZ would primarily depend on major fractures that could connect the different parts of the TZ (e.g. Faulkner et al., 2001). Nevertheless, natural seismic events have occurred in structures with the same orientation within the area (e.g. Häge et Joswig., 2009). The mix of quartz and clay along with the compartmentalisation of the RFZ make it extremely heterogeneous mechanically (Bedford et al., 2022). Aseismic and seismic slips could occur either naturally or induced during stimulation due to a local increase in pressure within the DZ of the TZ.

Comparing the ore vein to a pathway for a present-day geothermal brine illustrates how the RFZ influenced the fluid circulation. The ore vein is visible on both sides of the RFZ, but there is no evidence of ore deposit through the MCZ. Numerous veins were deposited with the same orientation as the ore vein, mainly in the gneiss (Fig. 3a and b). This orientation can be related to the impervious behaviour of the clayey gouge zones acting as a barrier. This is of key importance for geothermal applications because if such a clay-rich fault zone exists between the injection and the production wells, it might likely hinder the hydraulic connection between the boreholes.

For better characterisation of fluid flow applied to geothermal, fracture orientation and dipping should also be considered within the present-day regional stress field as it will affect the permeability of the fractures (Meixner et al., 2018) in terms of dilation tendency. The fracture density, the connectivity of the fractures, the permeability and the connected porosity at the mineral scale need to be further investigated to provide a better understanding of how a geothermal fluid would circulate in such a structure.

6. Conclusion

The RFZ presents a complex permeability and mechanical distribution related to its multi-core architecture and mineralogical composition. Through its formation, Variscan structures were reactivated and sheared with a WNW orientation, as well as the place for fluid/rock interaction. The RFZ samples showed evidence of deformation with fracturing, grain size reduction and cataclasis. They also show hydrothermal alteration evidence such as biotite and plagioclase transformation, quartz and calcite precipitation along clay formation. From the lower Jurassic to the lower Cretaceous, with a fault-valve behaviour, the repetition of the RFZ seismic cycle led to its widening with either mechanical strengthening or weakening. This is now highlighted within a mine gallery by the impervious clayey gouge zones which compartmentalise the TZ.

The RFZ influenced the formation of the perpendicular ore vein by playing a passive role. Under the NNE dextral transtensional shearing, the high clay content of the RFZ, especially the MCZ, led to a smearing of the structure without opening. Ascending fluid flowing on both sides of the RFZ (Fig. 9g) promoted the mineralisation and could explain the ore vein geometry.

Using the interaction between the RFZ and the ore vein as an analogue yields insight into present-day preferential fluid pathways within a multi-core fault zone. The DZs comprised between the vertical clayey gouge zones would be the most permeable structures at present. Still, a major structure crossing the clayey gouge zones would be necessary to ensure connectivity across the RFZ. These observations provide another recommendation for geothermal application by suggesting that the occurrence of wide clay-rich gouges between injection and production wells can strongly affect the hydraulic connectivity of the reservoir and impact the viability of a geothermal project.

CRediT authorship contribution statement

Benjamin Avakian: Writing – original draft, Visualization, Supervision, Software, Resources, Methodology, Investigation, Formal analysis, Data curation, Conceptualization. **Beatrice A. Ledesert:** Writing – review & editing, Validation, Project administration, Methodology, Funding acquisition, Data curation, Conceptualization. **Ghislain Trullenque:** Methodology, Funding acquisition, Conceptualization. **Ronan L. Hébert:** Writing – review & editing, Visualization, Validation, Methodology, Data curation, Conceptualization. **Johanne Klee:** Writing – review & editing, Software, Methodology. **Sébastien Potel:** Writing – review & editing, Validation, Data curation, Conceptualization. **Titouan Miloikovitch:** Software, Methodology. **Steven Goderis:** Writing – review & editing, Validation, Methodology, Data curation, Conceptualization. **Philippe Claeys:** Writing – review & editing, Validation, Project administration, Methodology, Funding acquisition, Data curation, Conceptualization.

Declaration of competing interest

The authors declare that they have no known competing financial interests or personal relationships that could have appeared to influence the work reported in this paper.

Acknowledgment

This project was supported by the EUTOPIA European University network which provided a PhD grant and the European Union's Horizon 2020 Research and Innovation program under grant agreement no. 792037 (H2020 MEET project). Philippe Claeys and Steven Goderis acknowledge support from Research Foundation Flanders for the acquisition of micro-XRF instrument and VUB Strategic Research. We would like to thank the SLB SRPC GeoServices/Surface Logging department for providing us with the opportunity to use the DRIFTS

instrument and Marie Fiot from Celsius Energy for her help with the spectral analysis. Many thanks to Marie Dupuis and Hicham Mellouk, students at CY Cergy Paris Université who participated to the measurement of the samples.

Appendix A. Supplementary data

Supplementary data to this article can be found online at https://doi.org/10.1016/j.jsg.2024.105296.

Data availability

Data will be made available on request.

References

Acosta, M., Violay, M., 2020. Mechanical and hydraulic transport properties of transverse-isotropic Gneiss deformed under deep reservoir stress and pressure conditions. Int. J. Rock Mech. Min. Sci. 130, 104235. https://doi.org/10.1016/j.ijrmms.2020.104235.

Altherr, R., Henes-Klaiber, U., Hegner, E., Satir, M., Langer, C., 1999. Plutonism in the variscan Odenwald (Germany): from subduction to collision. Int. J. Earth Sci. 88, 422–443. https://doi.org/10.1007/s005310050276.

Altherr, R., Holl, A., Hegner, E., Langer, C., Kreuzer, H., 2000. High-potassium, calc-alkaline I-type plutonism in the European Variscides: northern Vosges (France) and northern Schwarzwald (Germany). Lithos 50, 51–73. https://doi.org/10.1016/S0024-4937(99)00052-3.

Altherr, R., Hanel, M., Schwarz, W.H., Wimmenauer, W., 2019. Petrology and U–Pb zircon age of the variscan porphyroclastic rand granite at the southeastern margin of the central Schwarzwald gneiss complex (Germany). Int. J. Earth Sci. 108, 1879–1895. https://doi.org/10.1007/s00531-019-01738-2.

Altherr, R., Hepp, S., Klein, H., Hanel, M., 2021. Metabasic rocks from the Variscan Schwarzwald (SW Germany): metamorphic evolution and igneous protoliths. Int. J. Earth Sci. 110, 1293–1319. https://doi.org/10.1007/s00531-021-02016-w.

Baujard, C., Genter, A., Dalmais, E., Maurer, V., Hehn, R., Rosillette, R., Vidal, J., Schmittbuhl, J., 2017. Hydrothermal characterization of wells GRT-1 and GRT-2 in Rittershoffen, France: implications on the understanding of natural flow systems in the rhine graben. Geothermics 65, 255–268. https://doi.org/10.1016/j.geothermics.2016.11.001.

Bedford, J.D., Faulkner, D.R., Lapusta, N., 2022. Fault rock heterogeneity can produce fault weakness and reduce fault stability. Nat. Commun. 13, 326. https://doi.org/10.1038/s41467-022-27998-2.

Bense, V.F., Gleeson, T., Loveless, S.E., Bour, O., Scibek, J., 2013. Fault zone hydrogeology. Earth Sci. Rev. 127, 171–192. https://doi.org/10.1016/j.earscirev.2013.09.008.

Bergerat, F., 1985. Déformations cassantes et champs de contrainte tertiaires dans la plate-forme européenne. Université Pierre et Marie Curie-Paris VI (PhD Thesis).

Bertrand, L., Géraud, Y., Diraison, M., 2021. Petrophysical properties in faulted basement rocks: insights from outcropping analogues on the West European Rift shoulders. Geothermics 95, 102144. https://doi.org/10.1016/j.geothermics.2021.102144.

Bischoff, A., Heap, M.J., Mikkola, P., Kuva, J., Reuschlé, T., Jolis, E.M., Engström, J., Reijonen, H., Leskelä, T., 2024. Hydrothermally altered shear zones: a new reservoir play for the expansion of deep geothermal exploration in crystalline settings. Geothermics 118, 102895. https://doi.org/10.1016/j.geothermics.2023.102895.

Bleam, W.F., 2012. Clay mineralogy and clay chemistry. In: Soil and Environmental Chemistry. Elsevier, pp. 85–116. https://doi.org/10.1016/B978-0-12-415797-2.00003-0.

Bossennec, C., Géraud, Y., Böcker, J., Klug, B., Mattioni, L., Bertrand, L., Moretti, I., 2021. Characterisation of fluid flow conditions and paths in the Buntsandstein Gp. sandstones reservoirs, Upper Rhine Graben. BSGF - Earth Sci. Bull. 192, 35. https://doi.org/10.1051/bsgf/2021027.

Bossennec, C., Seib, L., Frey, M., Van Der Vaart, J., Sass, I., 2022. Structural architecture and permeability patterns of crystalline reservoir rocks in the northern upper rhine graben: insights from surface analogues of the Odenwald. Energies 15, 1310. https://doi.org/10.3390/en15041310.

Burg, J.P., Matte, Ph, Leyreloup, A., Marchand, J., 1984. Inverted metamorphic zonation and large-scale thrusting in the Variscan Belt: an example in the French Massif Central. SP (Sci. Prog.) 14, 47–61. https://doi.org/10.1144/GSL.SP.1984.014.01.05.

Caine, J.S., Evans, J.P., Forster, C.B., 1996. Fault zone architecture and permeability structure. Geol. 24, 1025. https://doi.org/10.1130/0091-7613(1996)024<1025:FZAAPS>2.3.CO;2.

Caine, J.S., Tomusiak, S.R.A., 2003. Brittle structures and their role in controlling porosity and permeability in a complex Precambrian crystalline-rock aquifer system in the Colorado Rocky Mountain Front Range. Geo. Society Am. Bull. 115 (1), 1410. https://doi.org/10.1130/B25088.

Callahan, O.A., Eichhubl, P., Olson, J.E., Davatzes, N.C., 2019. Fracture mechanical properties of damaged and hydrothermally altered rocks, dixie valley-stillwater Fault Zone, Nevada, USA. J. Geophys. Res. Solid Earth 124, 4069–4090. https://doi.org/10.1029/2018JB016708.

Callahan, O.A., Eichhubl, P., Davatzes, N.C., 2020. Mineral precipitation as a mechanism of fault core growth. J. Struct. Geol. 140, 104156. https://doi.org/10.1016/j.jsg.2020.104156.

Chabani, A., Trullenque, G., Ledésert, B.A., Klee, J., 2021. Multiscale characterization of fracture patterns: a case study of the Noble Hills range (Death Valley, ca, USA), application to geothermal reservoirs. Geosciences 11, 280. https://doi.org/10.3390/geosciences11070280.

Chauvet, A., 2019. Structural control of ore deposits: the role of pre-existing structures on the formation of mineralised vein systems. Minerals 9, 56. https://doi.org/10.3390/min9010056.

Choi, J.-H., Edwards, P., Ko, K., Kim, Y.-S., 2016. Definition and classification of fault damage zones: a review and a new methodological approach. Earth Sci. Rev. 152, 70–87. https://doi.org/10.1016/j.earscirev.2015.11.006.

Cuenot, N., Charléty, J., Dorbath, L., Haessler, H., 2006. Faulting mechanisms and stress regime at the European HDR site of Soultz-sous-Forêts, France. Geothermics 35, 561–575. https://doi.org/10.1016/j.geothermics.2006.11.007.

de Joussineau, G., 2023. The geometrical properties of fracture corridors. Tectonophysics 846, 229637. https://doi.org/10.1016/j.tecto.2022.229637.

De Winter, N.J., Claeys, P., 2017. Micro X-ray fluorescence (μ XRF) line scanning on Cretaceous rudist bivalves: a new method for reproducible trace element profiles in bivalve calcite. Sedimentology 64, 231–251. https://doi.org/10.1111/sed.12299.

Dezayes, C., Lerouge, C., Innocent, C., Lach, P., 2021. Structural control on fluid circulation in a graben system: constraints from the Saint Pierre Bois quarry (Vosges, France). J. Struct. Geol. 146, 104323. https://doi.org/10.1016/j.jsg.2021.104323.

Doubre, C., Meghraoui, M., Masson, F., Lambotte, S., Jund, H., Bès De Berc, M., Grunberg, M., 2022. Seismotectonics in Northeastern France and neighboring regions. Compt. Rendus Geosci. 353, 153–185. https://doi.org/10.5802/crgeos.80.

Duwiquet, H., Guillou-Frottier, L., Arbaret, L., Bellanger, M., Guillon, T., Heap, M.J., 2021. Crustal Fault zones (cfz) as geothermal power systems: a preliminary 3D thm model constrained by a multidisciplinary approach. Geofluids 1–24. https://doi.org/10.1155/2021/8855632, 2021.

Edel, J.-B., Whitechurch, H., Diraison, M., 2006. Seismicity wedge beneath the upper rhine graben due to backwards alpine push? Tectonophysics 428, 49–64. https://doi.org/10.1016/j.tecto.2006.08.009.

Edel, J.-B., Schulmann, K., 2009. Geophysical constraints and model of the "Saxothuringian and Rhenohercynian subductions – magmatic arc system" in NE France and SW Germany. Bull. Soc. Geol. Fr. 180, 545–558. https://doi.org/10.2113/gssgfbull.180.6.545.

Faulkner, D.R., Rutter, E.H., 2001. Can the maintenance of overpressured fluids in large strike-slip fault zones explain their apparent weakness? Geol. 29, 503. https://doi.org/10.1130/0091-7613(2001)029<0503:CTMOOF>2.0.CO;2.

Faulkner, D.R., Jackson, C.A.L., Lunn, R.J., Schlische, R.W., Shipton, Z.K., Wibberley, C. A.J., Withjack, M.O., 2010. A review of recent developments concerning the structure, mechanics and fluid flow properties of fault zones. J. Struct. Geol. 32, 1557–1575. https://doi.org/10.1016/j.jsg.2010.06.009.

Frey, M., Bär, K., Stober, I., Reinecker, J., Van Der Vaart, J., Sass, I., 2022. Assessment of deep geothermal research and development in the Upper Rhine Graben. Geoth. Energy 10, 18. https://doi.org/10.1186/s40517-022-00226-2.

Genter, A., Traineau, H., 1992. Borehole EPS-1, Alsace, France: preliminary geological results from granite core analyses for Hot Dry Rock research. Int. J. Rock Mech. Min. Sci. Geomech. Abstracts 3, 205–214. https://doi.org/10.1016/0148-9062(93)92984-X.

Genter, A., Traineau, H., Dezayes, Ch, Elsass, P., Ledesert, B., Meunier, A., Villemin, T., 1996. Fracture analysis and reservoir characterization of the granitic basement in the HDR Soultz Project (France). Int. J. Rock Mech. Min. Sci. Geomech. Abstracts 33, 189–214. https://doi.org/10.1016/0148-9062(96)83915-5.

Genter, A., Evans, K., Cuenot, N., Fritsch, D., Sanjuan, B., 2010. Contribution of the exploration of deep crystalline fractured reservoir of Soultz to the knowledge of enhanced geothermal systems (EGS). Compt. Rendus Geosci. 342, 502–516. https://doi.org/10.1016/j.crte.2010.01.006.

Geyer, O.F., Gwinner, M.P., Geyer, M., Nitsch, E., Simon, T., Ellwanger, D., 2011. Geologie von Baden-Württemberg, 5., völlig neu bearb. Aufl. Schweizerbart, Stuttgart.

Gillespie, P.A., Howard, C.B., Walsh, J.J., Watterson, J., 1993. Measurement and characterisation of spatial distributions of fractures. Tectonophysics 226, 113–141. https://doi.org/10.1016/0040-1951(93)90114-Y.

Glaas, C., Patrier, P., Vidal, J., Beaufort, D., Girard, J.-F., Genter, A., 2020. Hydrothermal alteration in the new deep geothermal well GIL-1 (strasbourg area, France). In: Proceedings World Geothermal Congress. Reykjavik, Iceland.

Glaas, C., Vidal, J., Genter, A., 2021. Structural characterization of naturally fractured geothermal reservoirs in the central Upper Rhine Graben. J. Struct. Geol. 148, 104370. https://doi.org/10.1016/j.jsg.2021.104370.

Häge, M., Joswig, M., 2009. Spatiotemporal distribution of aftershocks of the 2004 December 5 M L = 5.4 Waldkirch (Germany) earthquake. Geophys. J. Int. 178, 1523–1532. https://doi.org/10.1111/j.1365-246X.2009.04235.x.

Heidbach, O., Rajabi, M., Reiter, K., Ziegler, M., 2016. World stress map 2016. https://doi.org/10.5880/WSM.2016.002.

Herron, M., Loan, M., Charsky, A., Herron, S.L., Pomerantz, A.E., Polyakov, M., 2014. Clay typing, mineralogy, kerogen content and kerogen characterization from DRIFTS analysis of cuttings or core. In: Proceedings of the 2nd Unconventional Resources Technology Conference. Presented at the Unconventional Resources Technology Conference. American Association of Petroleum Geologists, Denver, Colorado, USA. https://doi.org/10.15530/urtec-2014-1922653.

Illies, J.H., 1967. Development and tectonic pattern of the Rhinegraben. In: Rothé, J.P., Sauer, K. (Eds.), The Rhinegraben Progress Report, vol. 6. Abh geol Landesamt Baden-Wütemberg, pp. 7–9.

Illies, J.H., Greiner, G., 1979. Holocene movements and state of stress in the rhinegraben Rift System. In: Developments in Geotectonics. Elsevier, pp. 349–359. https://doi.org/10.1016/B978-0-444-41783-1.50057-X.
Inoue, A., 1995. Formation of clay minerals in hydrothermal environments. In: Velde, B. (Ed.), Origin and Mineralogy of Clays: Clays and the Environment. Springer Berlin Heidelberg, Berlin, Heidelberg, pp. 268–329. https://doi.org/10.1007/978-3-662-12648-6_7.
Insua-Arévalo, J.M., Tsige, M., Sánchez-Roldán, J.L., Rodríguez-Escudero, E., Martínez-Díaz, J.J., 2021. Influence of the microstructure and roughness of weakness planes on the strength anisotropy of a foliated clay-rich fault gouge. Eng. Geol. 289, 106186. https://doi.org/10.1016/j.enggeo.2021.106186.
Kaskes, P., Déhais, T., de Graaff, S.J., Goderis, S., Claeys, P., 2021. Micro–X-ray fluorescence (μXRF) analysis of proximal impactites: high-resolution element mapping, digital image analysis, and quantifications. In: Reimold, W.U., Koeberl, C. (Eds.), Large Meteorite Impacts and Planetary Evolution VI. Geological Society of America, pp. 171–206. https://doi.org/10.1130/2021.2550(07.
Klee, J., Chabani, A., Ledésert, B.A., Potel, S., Hébert, R.L., Trullenque, G., 2021a. Fluid-rock interactions in a paleo-geothermal reservoir (Noble Hills granite, California, USA). Part 2: the influence of fracturing on granite alteration processes and fluid circulation at low to moderate regional strain. Geosciences 11, 433. https://doi.org/10.3390/geosciences11110433.
Klee, J., Potel, S., Ledésert, B.A., Hébert, R.L., Chabani, A., Barrier, P., Trullenque, G., 2021b. Fluid-rock interactions in a paleo-geothermal reservoir (Noble Hills granite, California, USA). Part 1: granite pervasive alteration processes away from fracture zones. Geosciences 11, 325. https://doi.org/10.3390/geosciences11080325.
Krohe, A., Eisbacher, G.H., 1988. Oblique crustal detachment in the Variscan Schwarzwald, southwestern Germany. Geol. Rundsch. 77, 25–43. https://doi.org/10.1007/BF01848674.
Lagarde, J.-L., Capdevila, R., Fourcade, S., 1992. Granites et collision continentale: l'exemple des granitoïdes carbonifères dans la chaîne hercynienne ouest-européenne. Bulletin-Societe Geologique De France 163, 597–597.
Lahiri, S., 2021. Estimating effective permeability using connectivity and branch length distribution of fracture network. J. Struct. Geol. 146, 104314. https://doi.org/10.1016/j.jsg.2021.104314.
Larroque, J.M., Etchecopar, A., Philip, H., 1987. Evidence for the permutation of stresses σ1 and σ2 in the Alpine foreland: the example of the Rhine graben. Tectonophysics 144, 315–322. https://doi.org/10.1016/0040-1951(87)90299-X.
Lê, S., Josse, J., Husson, F., 2008. FactoMineR : an R package for multivariate analysis. J. Stat. Software 25. https://doi.org/10.18637/jss.v025.i01.
Ledésert, B., Berger, G., Meunier, A., Genter, A., Bouchet, A., 1999. Diagenetic-type reactions related to hydrothermal alteration in the Soultz-sous-Forêts granite, France. ejm 11, 731–742. https://doi.org/10.1127/ejm/11/4/0731.
Ledésert, B., Hébert, R.L., Grall, C., Genter, A., Dezayes, C., Bartier, D., Gérard, A., 2009. Calcimetry as a useful tool for a better knowledge of flow pathways in the Soultz-sous-Forêts Enhanced Geothermal System. J. Volcanol. Geoth. Res. 181, 106–114. https://doi.org/10.1016/j.jvolgeores.2009.01.001.
Ledésert, B., Hebert, R., Genter, A., Bartier, D., Clauer, N., Grall, C., 2010. Fractures, hydrothermal alterations and permeability in the Soultz enhanced geothermal system. Compt. Rendus Geosci. 342, 607–615. https://doi.org/10.1016/j.crte.2009.09.011.
Loan, M.L., Herron, M.M., Matteson, A., Charsky, A., Prioul, R., Prange, M., 2017. Rapid quantification of mineralogy, organic matter, and thermal maturity of cuttings with Diffuse reflectance infrared fourier transform spectroscopy, permian basin. In: Proceedings of the 5th Unconventional Resources Technology Conference. Presented at the Unconventional Resources Technology Conference. American Association of Petroleum Geologists, Austin, Texas, USA. https://doi.org/10.15530/urtec-2017-2671423.
Meixner, J., Schill, E., Gaucher, E., Kohl, T., 2014. Inferring the in situ stress regime in deep sediments: an example from the Bruchsal geothermal site. Geoth. Energy 2, 7. https://doi.org/10.1186/s40517-014-0007-z.
Meixner, J., Schill, E., Grimmer, J.C., Gaucher, E., Kohl, T., Klingler, P., 2016. Structural control of geothermal reservoirs in extensional tectonic settings: an example from the Upper Rhine Graben. J. Struct. Geol. 82, 1–15. https://doi.org/10.1016/j.jsg.2015.11.003.
Meixner, J., Grimmer, J.C., Becker, A., Schill, E., Kohl, T., 2018. Comparison of different digital elevation models and satellite imagery for lineament analysis: implications for identification and spatial arrangement of fault zones in crystalline basement rocks of the southern Black Forest (Germany). J. Struct. Geol. 108, 256–268. https://doi.org/10.1016/j.jsg.2017.11.006.
Meller, C., Kohl, T., 2014. The significance of hydrothermal alteration zones for the mechanical behavior of a geothermal reservoir. Geoth. Energy 2, 12. https://doi.org/10.1186/s40517-014-0012-2.
Meller, C., Kontny, A., Kohl, T., 2014. Identification and characterization of hydrothermally altered zones in granite by combining synthetic clay content logs with magnetic mineralogical investigations of drilled rock cuttings. Geophys. J. Int. 199, 465–479. https://doi.org/10.1093/gji/ggu278.
Meller, C., Ledésert, B., 2017. Is there a link between mineralogy, petrophysics, and the hydraulic and seismic behaviors of the soultz-sous-forêts granite during stimulation? A review and reinterpretation of petro-hydromechanical data toward a better understanding of induced seismicity: petro-hydromechanics of Soultz granite. J. Geophys. Res. Solid Earth 122, 9755–9774. https://doi.org/10.1002/2017JB014648.
Peacock, D.C.P., Sanderson, D.J., Leiss, B., 2022. Use of analogue exposures of fractured rock for enhanced geothermal systems. Geosciences 12, 318. https://doi.org/10.3390/geosciences12090318.
Pfaff, K., Romer, R.L., Markl, G., 2009. U-Pb ages of ferberite, chalcedony, agate, "U-mica" and pitchblende: constraints on the mineralization history of the Schwarzwald ore district. Eur. J. Mineral 21, 817–836. https://doi.org/10.1127/0935-1221/2009/0021-1944.
Robion, P., David, C., Dautriat, J., Colombier, J.-C., Zinsmeister, L., Collin, P.-Y., 2014. Pore fabric geometry inferred from magnetic and acoustic anisotropies in rocks with various mineralogy, permeability and porosity. Tectonophysics 629, 109–122. https://doi.org/10.1016/j.tecto.2014.03.029.
Rotstein, Y., Schaming, M., 2011. The Upper Rhine Graben (URG) revisited: Miocene transtension and transpression account for the observed first-order structures: transpression in the upper rhine graben. Tectonics 30, 3. https://doi.org/10.1029/2010TC002767.
Rutter, E.H., Maddock, R.H., Hall, S.H., White, S.H., 1986. Comparative microstructures of natural and experimentally produced clay-bearing fault gouges. PAGE 124, 3–30. https://doi.org/10.1007/BF00875717.
Savage, H.M., Brodsky, E.E., 2011. Collateral damage: evolution with displacement of fracture distribution and secondary fault strands in fault damage zones. J. Geophys. Res. 116, B03405. https://doi.org/10.1029/2010JB007665.
Schmittbuhl, J., Lambotte, S., Lengliné, O., Grunberg, M., Jund, H., Vergne, J., Cornet, F., Doubre, C., Masson, F., 2022. Induced and triggered seismicity below the city of strasbourg, France from november 2019 to january 2021. Comptes rendus. Geoscience 353, 561–584. https://doi.org/10.5802/crgeos.71.
Schuck, B., Schleicher, A.M., Janssen, C., Toy, V.G., Dresen, G., 2020. Fault zone architecture of a large plate-bounding strike-slip fault: a case study from the Alpine Fault, New Zealand. Solid Earth 11, 95–124. https://doi.org/10.5194/se-11-95-2020.
Schulz, K.E., Bär, K., Sass, I., 2022. Lab-scale permeability enhancement by chemical treatment in fractured granite (cornubian batholith) for the united downs deep geothermal power project, cornwall (UK). Geosciences 12, 35. https://doi.org/10.3390/geosciences12010035.
Schumacher, M.E., 2002. Upper Rhine Graben: role of preexisting structures during rift evolution: upper rhine graben evolution. Tectonics 21. https://doi.org/10.1029/2001TC900022, 6-1-6–17.
Sibson, R.H., 1977. Fault rocks and fault mechanisms. JGS 133, 191–213. https://doi.org/10.1144/gsjgs.133.3.0191.
Sibson, R.H., 1992. Implications of fault-valve behaviour for rupture nucleation and recurrence. Tectonophysics 211, 283–293. https://doi.org/10.1016/0040-1951(92)90065-E.
Sibson, R.H., 2007. An episode of fault-valve behaviour during compressional inversion? — The 2004 MJ6.8 Mid-Niigata Prefecture, Japan, earthquake sequence. Earth Planet Sci. Lett. 257, 188–199. https://doi.org/10.1016/j.epsl.2007.02.031.
Sittler, C., 1985. Les hydrocarbures d'Alsace dans le contexte historique et géodynamique du fossé rhénan. Bulletin des Centres de Recherches Elf Exploration Production 2, 335–371.
Staude, S., Bons, P.D., Markl, G., 2009. Hydrothermal vein formation by extension-driven dewatering of the middle crust: an example from SW Germany. Earth Planet Sci. Lett. 286, 387–395. https://doi.org/10.1016/j.epsl.2009.07.012.
Sutherland, R., Toy, V.G., Townend, J., Cox, S.C., Eccles, J.D., Faulkner, D.R., Prior, D.J., Norris, R.J., Mariani, E., Boulton, C., Carpenter, B.M., Menzies, C.D., Little, T.A., Hasting, M., De Pascale, G.P., Langridge, R.M., Scott, H.R., Lindroos, Z.R., Fleming, B., Kopf, A.J., 2012. Drilling reveals fluid control on architecture and rupture of the Alpine fault, New Zealand. Geology 40, 1143–1146. https://doi.org/10.1130/G33614.1.
Torabi, A., Ellingsen, T.S.S., Johannessen, M.U., Alaei, B., Rotevatn, A., Chiarella, D., 2020. Fault zone architecture and its scaling laws: where does the damage zone start and stop? Geological Society 496, 99–124. https://doi.org/10.1144/SP496-2018-151. London, Special Publications.
Vidal, J., Genter, A., Chopin, F., 2017. Permeable fracture zones in the hard rocks of the geothermal reservoir at Rittershoffen, France. JGR Solid Earth 122, 4864–4887. https://doi.org/10.1002/2017JB014331.
Vidal, J., Genter, A., 2018. Overview of naturally permeable fractured reservoirs in the central and southern Upper Rhine Graben: insights from geothermal wells. Geothermics 74, 57–73. https://doi.org/10.1016/j.geothermics.2018.02.003.
Villemin, T., Bergerat, F., 1987. L'evolution structurale du fosse rhenan au cours du Cenozoique ; un bilan de la deformation et des effets thermiques de l'extension. Bull. Soc. Geol. Fr. III, 245–255. https://doi.org/10.2113/gssgfbull.III.2.245.
Walter, B.F., Immenhauser, A., Geske, A., Markl, G., 2015. Exploration of hydrothermal carbonate magnesium isotope signatures as tracers for continental fluid aquifers, Schwarzwald mining district, SW Germany. Chem. Geol. 400, 87–105. https://doi.org/10.1016/j.chemgeo.2015.02.009.
Walter, B.F., Burisch, M., Markl, G., 2016. Long-term chemical evolution and modification of continental basement brines - a field study from the Schwarzwald, SW Germany. Geofluids 16, 604–623. https://doi.org/10.1111/gfl.12167.
Walter, B.F., Kortenbruck, P., Scharrer, M., Zeitvogel, C., Wälle, M., Mertz-Kraus, R., Markl, G., 2019. Chemical evolution of ore-forming brines – basement leaching, metal provenance, and the redox link between barren and ore-bearing hydrothermal veins. A case study from the Schwarzwald mining district in SW-Germany. Chem. Geol. 506, 126–148. https://doi.org/10.1016/j.chemgeo.2018.12.038.
Werner, W., Franzke, H.J., Wirsing, G., Jochum, J., Steiber, B., 2002. Bergbau, Geologie, Hydrogeologie, Mineralogie, Geochemie, Tektonik und Lagerstättenentstehung, vol. 114.
Whitney, D.L., Evans, B.W., 2010. Abbreviations for names of rock-forming minerals. Am. Mineral. 95, 185–187. https://doi.org/10.2138/am.2010.3371.
Wibberley, C.A.J., Shimamoto, T., 2003. Internal structure and permeability of major strike-slip fault zones: the median tectonic line in mie prefecture, southwest Japan. J. Struct. Geol. 25, 59–78. https://doi.org/10.1016/S0191-8141(02)00014-7.

Wibberley, C.A.J., Yielding, G., Di Toro, G., 2008. Recent advances in the understanding of fault zone internal structure: a review. Geological Society, London, Special Publications 299, 5–33. https://doi.org/10.1144/SP299.2.

Wittenbrink, J., 1999. Diplomkartierung (Teil A) Petrographische und tektonische Kartierung des Zentralschwarzwälder Gneiskomplexes im Bereich der Blei – Zink – Lagerstätte Schauinsland bei Freiburg i. Br./Schwarzwald (Master Thesis). Technische Universität Clausthal.

Ziegler, P.A., 1992. European Cenozoic rift system. Tectonophysics 208, 91–111. https://doi.org/10.1016/0040-1951(92)90338-7.

Ziegler, P.A., Dèzes, P., 2005. Evolution of the lithosphere in the area of the rhine Rift System. Int. J. Earth Sci. 94, 594–614. https://doi.org/10.1007/s00531-005-0474-3.

Ziegler, P.A., Schumacher, M.E., Dèzes, P., Van Wees, J.-D., Cloetingh, S., 2006. Post-variscan evolution of the lithosphere in the area of the European Cenozoic Rift System. Memoir 32, 97–112. https://doi.org/10.1144/GSL.MEM.2006.032.01.06.